REPORT DOCUMENTATION PAGE

1. REPORT DATE (DD-MM-YYYY) 05-10-2013	2. REPORT TYPE	3. DATES COVERED (From - To)

4. TITLE AND SUBTITLE

Towing Tank Measurements of Hydrodynamic Performance of a Horizontal Axis Tidal Turbine Under Unsteady Flow Conditions

5a. CONTRACT NUMBER

5b. GRANT NUMBER

5c. PROGRAM ELEMENT NUMBER

6. AUTHOR(S)
Van Benthem, Max Cullen

5d. PROJECT NUMBER

5e. TASK NUMBER

5f. WORK UNIT NUMBER

7. PERFORMING ORGANIZATION NAME(S) AND ADDRESS(ES)

8. PERFORMING ORGANIZATION REPORT NUMBER

9. SPONSORING / MONITORING AGENCY NAME(S) AND ADDRESS(ES)
U.S. Naval Academy
Annapolis, MD 21402

10. SPONSOR/MONITOR'S ACRONYM(S)

11. SPONSOR/MONITOR'S REPORT NUMBER(S)
Trident Scholar Report no. 423 (2013)

12. DISTRIBUTION / AVAILABILITY STATEMENT

This document has been approved for public release; its distribution is UNLIMITED.

13. SUPPLEMENTARY NOTES

14. ABSTRACT

Tidal turbines harness hydrokinetic energy resulting from ocean tidal flows to generate power. This type of power generation is a potential source of clean, reliable renewable energy. However, the technology is still under development. The effects of unsteady flow conditions, specifically surface gravity waves, on tidal turbines have not been completely analyzed. The effects of waves on performance characteristics were assessed for a model horizontal axis tidal turbine selected by the Department of Energy and designed by the National Renewable Energy Laboratory (NREL). The performance characteristics of the 1/25th scale model turbine were tested under unsteady flow conditions. Parameters including wave height, wave length and tow speed for the experiment were scaled to properly model flow conditions that a horizontal axis tidal turbine was expected to experience at a full scale. First, turbine rotational speed, torque and thrust were measured for steady flow conditions and unsteady flow conditions characterized by a range of incoming waves. Turbine performance characteristics, including thrust and power coefficients, were obtained as functions of rotor tip speed ratio for the unsteady flow conditions tested. The second experiment involved a detailed fluid flow survey in the near wake of the turbine with and without one of the waves utilized in the first experiment, as measured by Acoustic Doppler Velocimeters. The results provided a characterization of velocity fields in the near wake of the turbine, necessary information for the placement of multiple turbines in a larger array.

15. SUBJECT TERMS
Tidal Turbine Performance, Waves, Near Wake Turbulence

16. SECURITY CLASSIFICATION OF:			17. LIMITATION OF ABSTRACT	18. NUMBER OF PAGES	19a. NAME OF RESPONSIBLE PERSON
a. REPORT	b. ABSTRACT	c. THIS PAGE		47	19b. TELEPHONE NUMBER (include area code)

TOWING TANK MEASUREMENTS OF HYDRODYNAMIC PERFORMANCE OF A HORIZONTAL AXIS TIDAL TURBINE UNDER UNSTEADY FLOW CONDITIONS

by

Midshipman 1/c Max C. Van Benthem
United States Naval Academy
Annapolis, Maryland

_____

Certification of Advisers' Approval

Assistant Professor Luksa Luznik
Mechanical Engineering Department

_____

_____

Professor Karen Flack
Mechanical Engineering Department

_____

_____

Acceptance for the Trident Scholar Committee

Professor Maria J. Schroeder
Associate Director of Midshipman Research

_____

_____

USNA-1531-2

Abstract

Tidal turbines harness hydrokinetic energy resulting from ocean tidal flows to generate power. This type of power generation is a potential source of clean, reliable renewable energy. However, the technology is still under development. The effects of unsteady flow conditions, specifically surface gravity waves, on tidal turbines have not been completely analyzed. The effects of waves on performance characteristics were assessed for a model horizontal axis tidal turbine selected by the Department of Energy and designed by the National Renewable Energy Laboratory (NREL). The performance characteristics of the 1/25th scale model turbine were tested under unsteady flow conditions. The experiments were conducted in the large tow tank facility at the United States Naval Academy Hydromechanics Laboratory. Parameters including wave height, wave length and tow speed for the experiment were scaled to properly model flow conditions that a horizontal axis tidal turbine was expected to experience at a full scale. Two different experiments were conducted. First, turbine rotational speed, torque and thrust were measured for steady flow conditions and unsteady flow conditions characterized by a range of incoming waves. Wave types were varied to represent different flow conditions. Experiments were repeated at two different turbine immersion depths. Turbine performance characteristics, including thrust and power coefficients, were obtained as functions of rotor tip speed ratio for the unsteady flow conditions tested. Power generation was presented as a function of wave phase. The second experiment involved a detailed fluid flow survey in the near wake of the turbine with and without one of the waves utilized in the first experiment. Fluid flow was measured using Acoustic Doppler Velocimeters. The results of the experiment provided a characterization of velocity fields in the near wake of the turbine, necessary information for the placement of multiple turbines in a larger array.

Keywords

Acknowledgements

Table of Contents

I. Introduction

Renewable energy is a topic of increasing interest in the 21st Century. As a result of trends in the global climate, there is demand for energy with reduced emissions of greenhouse gasses [1]. Various methods of harnessing the bountiful energy pools in nature are in development. Wind energy and solar energy have received the most public attention. Much research has been conducted in these areas. However, the oceans also contain a large amount of available energy. Marine hydrokinetic energy devices are gaining increasing attention as a source of renewable energy. The two major sources of energy in the ocean are waves and tides. Waves are produced naturally by wind and several types of power generators have been developed to harness the energy of periodically oscillating waves [2]. Tidal flows are generated by the gravitational pull of the Moon and the Sun on the ocean. The result is a horizontal flow of water inland, the flood, and a return out to sea, the ebb. Tides are predictable because of the known orbital position of the moon and are tabulated by the National Ocean and Atmospheric Administration (NOAA) [3]. Tidal flows are a more dependable energy source than wind or sunlight, which are not as predictable and can be affected by other environmental factors such as clouds.

The Navy has expressed interest in increasing the use of renewable energy sources. In a speech at the Naval Energy Forum in 2009, the Secretary of the Navy, the Honorable Ray Mabus, stated five energy targets for the United States Navy. Two of the targets were directly related to the development of methods to harness tidal energy. The fourth target stated that 50% of shore-based energy will be obtained from renewable sources by 2020. The fifth demanded that 50% of all energy consumption be obtained from renewable sources by 2020 [4]. Naval bases are located near areas optimal for tidal energy collection devices. The development of tidal hydrokinetic energy technology assists the Navy in achieving its stated energy goals.

The energy conversion of tidal turbines is similar to that of wind turbines. Tidal turbines capture the kinetic energy in the water during flood and ebb tidal flows. In comparison to wind turbines, marine turbines have much higher power densities because the density of water is 800 times the density of air [5]. While wind turbines are a well-developed technology with many commercial applications, tidal turbines are still in the research and development phase.

The U.S. Department of Energy has funded a full research study of tidal turbines. The study requires the examination of a representative turbine modeled after Sea-Gen, the only operational tidal turbine in the world, installed near Strangford Lough in Northern Ireland. The Sea-Gen design contains two horizontal axis turbines mounted on either side of a supporting shaft, see Figure 1. The turbines each have two blades spaced 180° apart. The Sea-Gen turbine rotors are 20m diameter, 1.2 MW rated machines, see Figure 2. The rotors turn at ten to fifteen revolutions per minute in an average current speed of 2.4 m/s. Each turbine can develop 10MWh per tide which equates to around 6000 MWh per year. This is comparable to the energy produced by a 2.4 MW wind turbine in a year. Tidal turbines can produce twice the energy of wind turbines with the same power rating because of the higher power density of water and the reliability of the tides, opposed to the irregularity of the wind. [7].

Identifying and characterizing realistic flow fields is fundamental to understanding the operating conditions of tidal turbines. Surface waves impact the torque and power output of tidal turbines [8, 9]. Field measurements in the Chesapeake Bay estuary, at a depth corresponding to a turbine hub height, show that the presence of surface gravity waves can substantially alter the flow field experienced by the rotor blades [10]. A tidal turbine with a 20 m diameter rotor deployed in an estuary at a depth of 30 m typically encounters wind generated waves with a 3 second period and a wave height of 0.5 m. It follows from the wave model [11] that about 50% of the upper rotor swept area experiences unsteady wave velocities with magnitudes around 0.1 m/s, which could be several orders of magnitude larger than the ambient turbulence. Thus, tidal turbines are exposed to

unbalanced cyclic loading producing a time dependent flow on the turbine blades varying at the period of the incoming waves.
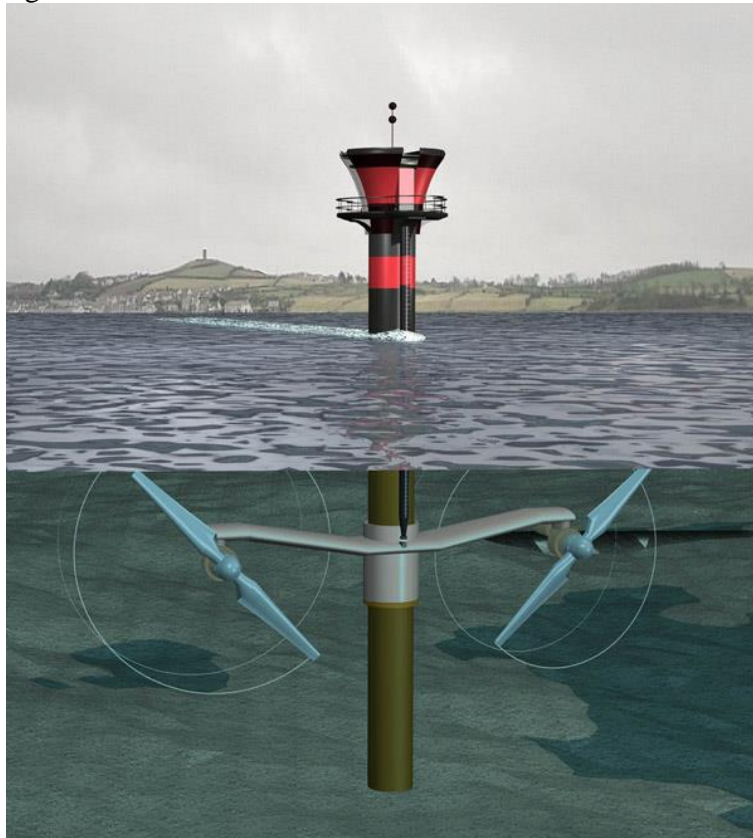

Figure 1: Sea-Gen twin turbines, with two blade configuration, harness the energy of ocean tidal flows. Artist's impression [6]
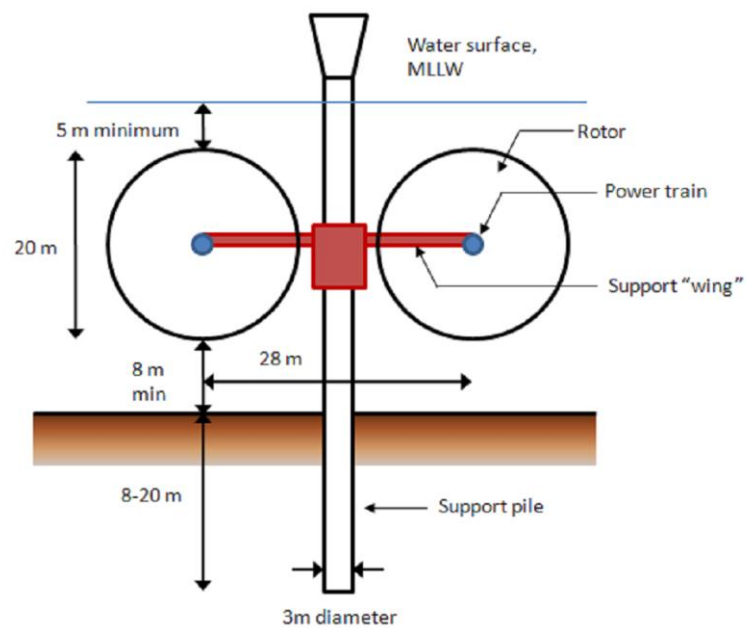

Figure 2: Reference horizontal axis turbine designed by NREL [12].

The Trident research project experimentally evaluated performance of a 1/25th scale horizontal axis tidal turbine model under unsteady flow conditions generated by surface gravity waves. The turbine model used during experimentation was a scaled version of a representative horizontal axis turbine designed by the National Renewable Energy Laboratory (NREL) based on the Sea-Gen prototype. Experiments were conducted in the large towing tank facility at the United States Naval Academy Hydromechanics Laboratory.

A. Hydrodynamics of Turbine Operation

Tidal turbines generate power using the kinetic energy of tidal flows. The turbine structural support is submerged and fixed to the ocean floor. The flow of water around the blades of the turbine due to the ebb and flood flows turns the turbine. The turning blades transmit torque to a shaft, which is connected to an electric generator. The generator converts the mechanical energy of the rotating shaft into electrical energy.

The blades generate torque using the same principles an airplane uses to remain in the air. The blades act as hydrofoils, creating lift and using the lift to turn the shaft. The analysis of the lifting force from a hydrofoil is complex, but the basic concept involves the relationship between velocity and pressure. The law of conservation of energy for inviscid, steady flow (Bernoulli's equation) states that the total amount of energy in a system must remain constant. In order to satisfy this requirement, an increase in the kinetic energy of the fluid due to increased velocity results in a decrease in pressure. On the blades of the turbine, the velocity over the suction (low pressure) side of the turbine blade is greater than the velocity over the pressure side. The simple explanation of this observed phenomenon comes from the law of conservation of mass in an open system, which states that mass flowing into the system must equal the mass flowing out of the system. The area through which the fluid must travel over the blade is decreased by the contoured shape of the blade. The resulting compression of the fluid can be represented by the behavior of streamlines. A streamline is the path that a particle of the fluid will travel in the system. On the suction side of the turbine blade, the streamlines are pressed closer together. The velocity of the fluid traveling over the suction side of the blade must increase in order to conserve the mass flow rate of the closer streamlines.

As stated above, the increase in fluid velocity over the suction side of the blade due to the shape results in a decrease in pressure. The pressure differential between the suction and pressure sides of the blade results in a lift force from the area of high pressure towards the area of low pressure. Because the turbine blade is fixed at one end to the shaft, the lift force on the blade results in a torque on the shaft. Therefore, the tidal turbine turns as a result of the hydrodynamic force on the blades from the flowing tides.

Figure 3 is a sketch of the flow of water around a turbine blade. The turbine blade is pictured coming up out of the page attached to the shaft into the page. The blade moves radially from the top of the page to the bottom of the page. The resulting velocity vector of the water seen by the turbine blade is $\omega R'$, where ω is the rotational speed of the turbine and R' is the distance from the turbine blade cross section to the turbine centerline. The inflow velocity of the tide, U_{in}, flows from left to right. The turbine blade is positioned at a specified angle of attack, α, to the incoming flow. The observed fluid velocity at the turbine blade is U_R, the relative velocity, the vector sum of $\omega R'$ and U_{in}. On the pressure side of the blade, the velocity does not experience a large change. On the suction side, the compression of the fluid streamlines results in a higher velocity. The increase in velocity correlates to a decrease in pressure by Bernoulli's equation. The higher pressure on the pressure side results in a lift force, F, towards the suction side, from higher pressure to lower pressure. F_R is the portion of lift force that causes the rotational movement of the blade. F_T is the thrust force on the turbine, the other component of the lift force. The lifting force on the blade results

in a torque, Q, on the shaft calculated by equation 1, where R′ is the distance the combined force on the turbine blade acts from the shaft centerline. The power developed by the turbine is calculated by equation 2. Not pictured for simplicity in Figure 3 is the drag force perpendicular to the lifting force. The drag force tends to decrease torque and increase thrust.

$$Q = F_R R' \qquad\qquad 1$$

$$Power = Q\omega \qquad\qquad 2$$
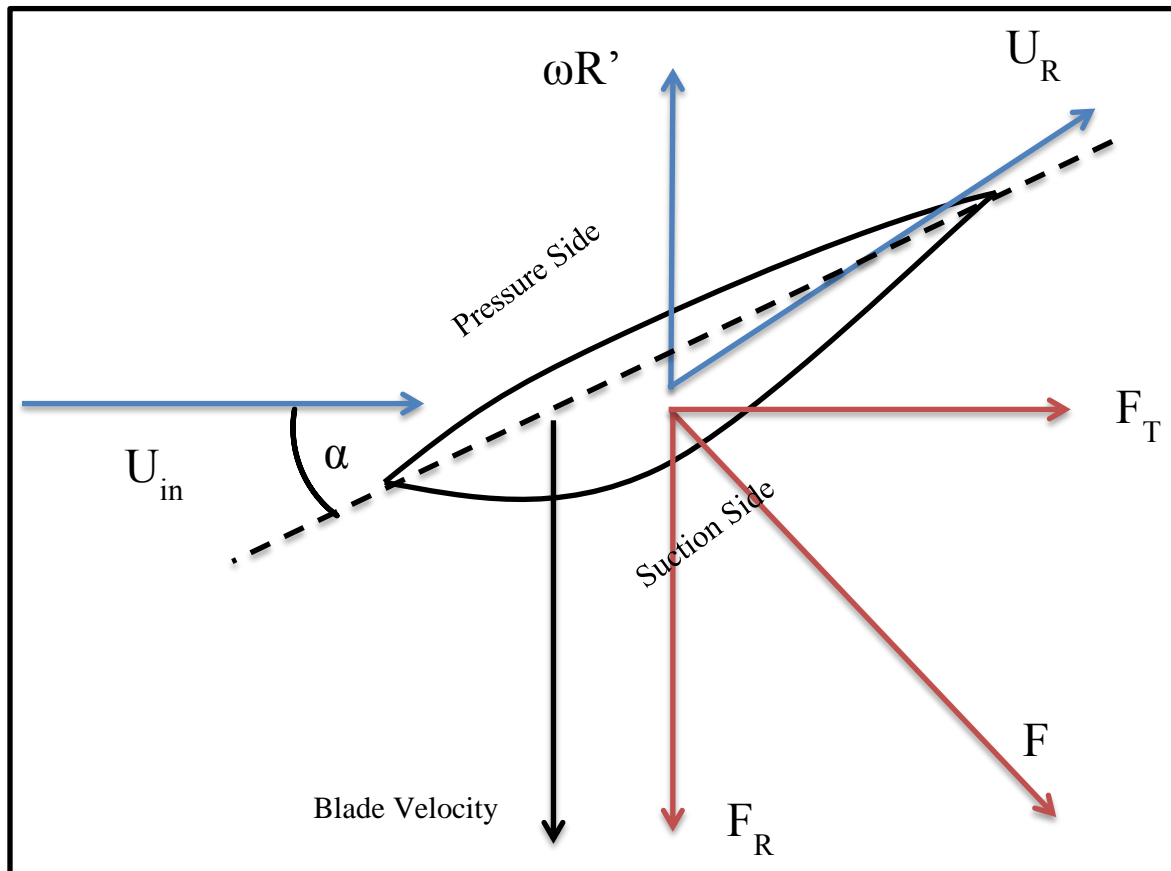
Figure 3: Flow around the blade of a tidal turbine results in lift force, FR, turning turbine blade.

The rotation of the turbine blades causes variations in the flow of the water. It is important that the effects of the turbine on the surrounding water are understood in order to include multiple turbines in a larger array. Large amounts of turbulence in the wake of a tidal turbine severely limits the minimum distance required between turbines to allow the flow to calm before entering the next turbine. Understanding the power generation of tidal turbines in an array requires knowledge of the flow patterns around a tidal turbine. Flow patterns in the near wake of a model tidal turbine were examined during the Trident research project.

II. Experimental Methods

A. United States Naval Academy Model Turbine

The model turbine used for experimentation is shown in Figure 4. It was designed by the Trident advisors in collaboration with NREL and fabricated by the Hydromechanics Lab technical staff. The model turbine was built during the summer of 2012. The model is 0.8 m in diameter, $1/25^{th}$ scale of the Sea-Gen prototype. It has a NACA 63-618 foil cross section with 13° twist, 62% taper, and is fabricated out of 6061 aluminum and anodized for corrosion resistance. The selected foil cross section demonstrated Reynolds number independence in the lift and drag coefficients for the velocity range tested during experimentation, explained in the following section [13]. Design and manufacture of the turbine was completed prior to the start of the Trident project.
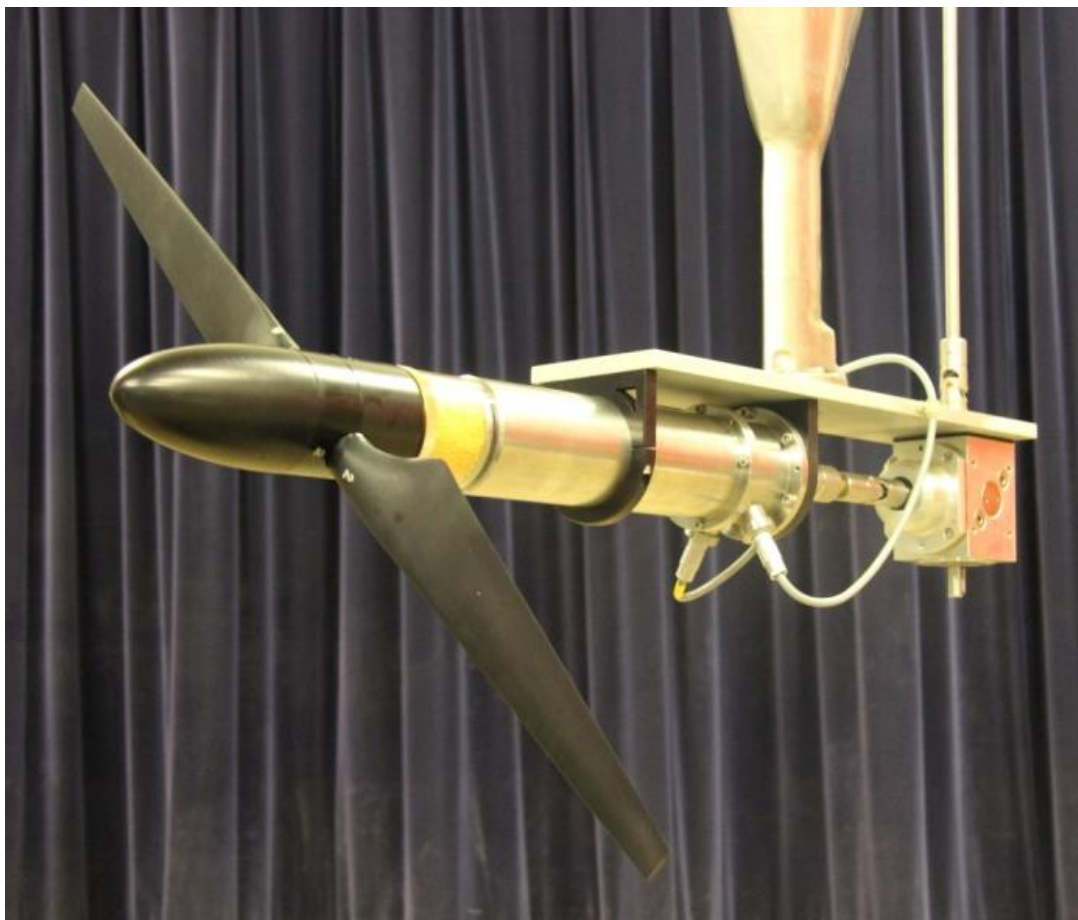
Figure 4: Model turbine (D = 0.8 m) showing two blades, hub, part of the support strut, and dynamometer housing used in the experiment.

B. Experimental Overview

Two sets of experiments were conducted in the 116 m Hydromechanics laboratory towing tank, as shown in Figure 5. The motivation for the first set of experiments was to determine the effects of flow unsteadiness on performance characteristics of the model turbine. Performance characteristics of the model turbine were the power coefficient, C_p, the thrust coefficient, C_T, and the tip speed ratio, TSR, all non-dimensional parameters. C_P represents the power developed by the turbine as a fraction of total available power of the flowing water (equation 3). The total available power is the dynamic

pressure, $\frac{1}{2}\rho U_{tow}{}^2$, times turbine rotor disk area, πR^2, times the fluid speed, U_{tow}, where ρ is fluid density. The maximum power that can be developed by a tidal turbine is 59.3% of the total available power. The theoretical limit termed the Betz limit is derived from the conservation of momentum [14]. C_T represents the thrust developed by the turbine as a fraction of the total hydrodynamic force available from the inflow to the turbine rotor disk area, calculated as the dynamic pressure of the fluid times the turbine rotor disk area (equation 4). The performance curves for the tidal turbine included C_P and C_T as a functions of TSR [14]. TSR is a ratio of the velocity at the tip to the tow speed (equation 5).

$$C_P = \frac{Power}{\frac{1}{2}\rho U_{tow}^3 \pi R^2} \qquad\qquad 3$$

$$C_T = \frac{Thrust}{\frac{1}{2}\rho U_{tow}^2 \pi R^2} \qquad\qquad 4$$

$$TSR = \frac{\omega R}{U_{tow}} \qquad\qquad 5$$

The turbine model was towed by the tow tank carriage at a constant tow speed, U_{tow} =1.68 m/s, for each run. The tow speed selection was a compromise between achieving the largest possible Reynolds number and operating within load limits for the measuring instrumentation discussed in the following section. The Reynolds number, Re, is a ratio of the body forces of a fluid to the viscous forces (equation 6).

$$Re = \frac{U_{0.7R} L_{chord}}{\nu} \qquad\qquad 6$$

$$U_{0.7R}^2 = U_{tow}^2 + (0.7R\omega)^2 \qquad\qquad 7$$

L_{chord} is the chord length at 0.7R, and ν is the kinematic viscosity of the fluid. Matching the Reynolds number of the model to the full scale turbine was desirable for modeling transitional and turbulent flow properly. The load limits of the equipment prevented matching Reynolds numbers. The Reynolds number based on relative velocity $U_{0.7R}$ calculated from tow speed, U_{tow}, and rotational velocity at 0.7R, as defined in equation 7, for the model turbine was 4×10^5. The range of TSR varied from 5.5 to 11.5 in order to locate the maximum power coefficient for the turbine [15]. An electromagnetic brake attached to the turbine shaft kept the rotation speed, ω, constant throughout the run. The voltage applied to the electromagnetic brake was varied to adjust the rotational speed from run to run. Two incoming wave conditions characterized by wave height and frequency combinations were selected for the first set of experiments based on wave scaling, discussed in summary of wave scaling. Waves were generated by the wavemaker in the tow tank. The turbine was towed in the opposite direction of the incoming waves, as shown in Figure 5. The procedure was repeated for two different turbine tip immersion depths: 0.8D and 1.8D, shown in Figure 5. The designation for these depths meant that the tip of the turbine blade at its closest position to the free surface of the water was 0.8 times and 1.6 times the diameter of the turbine.

The second set of experiments was conducted to characterize near wake flow structure under steady and unsteady flow conditions. For the near wake survey, all experiments were conducted at a fixed TSR of 7.2. An Acoustic Doppler Velocimeter (ADV) sensor was used to measure fluid velocities and was relocated after each run in order to provide spatial coverage of the wake velocities. This second set of experiments was motivated by the application of multiple tidal turbines in an

array. The near wake flow structure of a tidal turbine was measured and analyzed. Additionally, the impact of waves on the flow patterns around a tidal turbine was studied.
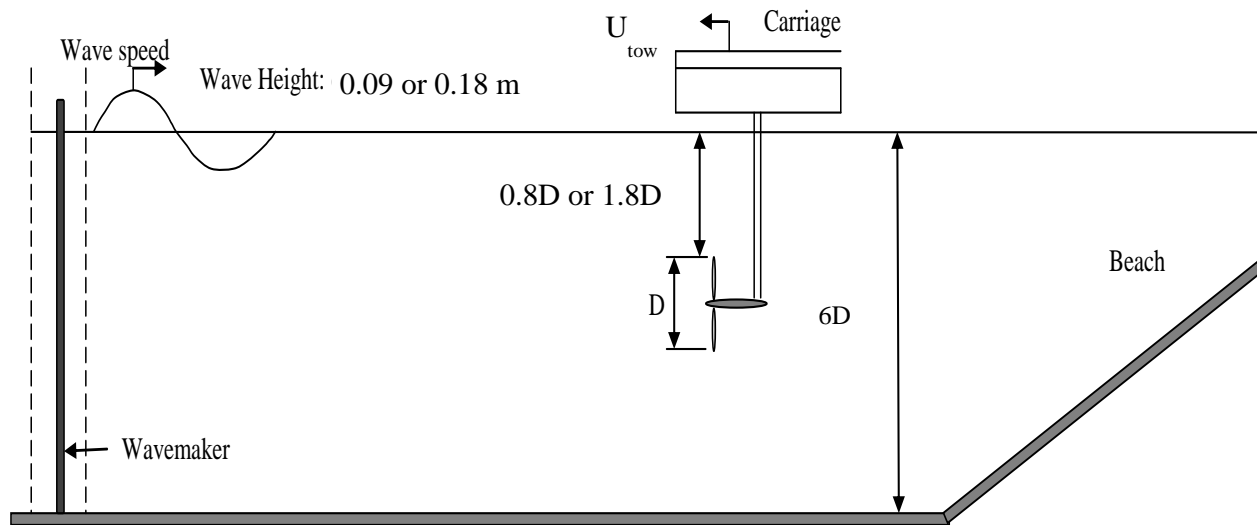

Figure 5: Sketch of the unsteady inflow towing tank experiment. Turbine model diameter, D= 0.8 m. Tank depth, h, was 4.9m (~6D).

C. Instrumentation

Table 1 summarizes the instrumentation used in the two sets of experiments, and the experimental set-up is shown in Figures 6 and 7. The thrust, T, and torque, Q, developed by the model turbine were measured with a Cussons Technology R46-01 Propulsion Dynamometer with limits of 700 N for thrust and 40 N-m for torque. A BEI Sensors H25 incremental optical encoder was specifically purchased for this project. It was attached to the vertical shaft connecting the dynamometer to the optical encoder and provided high resolution measurement of turbine rotational speed. It sent out 32000 pulses per revolution, which were received by sensors on the opposite side of a perforated disk. The pattern of pulses received was analyzed to determine the angular position. The number of counts per revolution equated to 88 pulses per degree. Therefore, the angular position of each turbine blade was determined to within 0.01136 degree resolution [16]. Additionally, a single analog pulse was recorded every time the reference turbine blade passed through the top dead center position. The recorded position of the turbine was designated as the "Z-pulse." In order to determine wave elevation, two Senix Optical Wave Height Sensors were rigidly attached to the towing carriage. They were positioned above the water free surface and in the plane of the rotor, as pictured in Figure 6. One sensor was located two diameters from the turbine centerline (on the starboard side), and the other towards the outer edge of the tow tank. These devices sent out an acoustic signal which was reflected by the free surface. The time between the emission of the signal and the return was used to determine the wave height. A Placid Industries, Inc. H250 hysteresis brake was used to control the rotational speed of the turbine and to absorb the power developed by the turbine. User input specified the voltage applied, which applied torque on the shaft. The brake controlled the rotational speed of the turbine. To monitor structural vibrations from the carriage, three single axis accelerometers were attached to the turbine strut just above the free surface. Each accelerometer was positioned in a different direction to measure longitudinal, vertical and lateral acceleration.
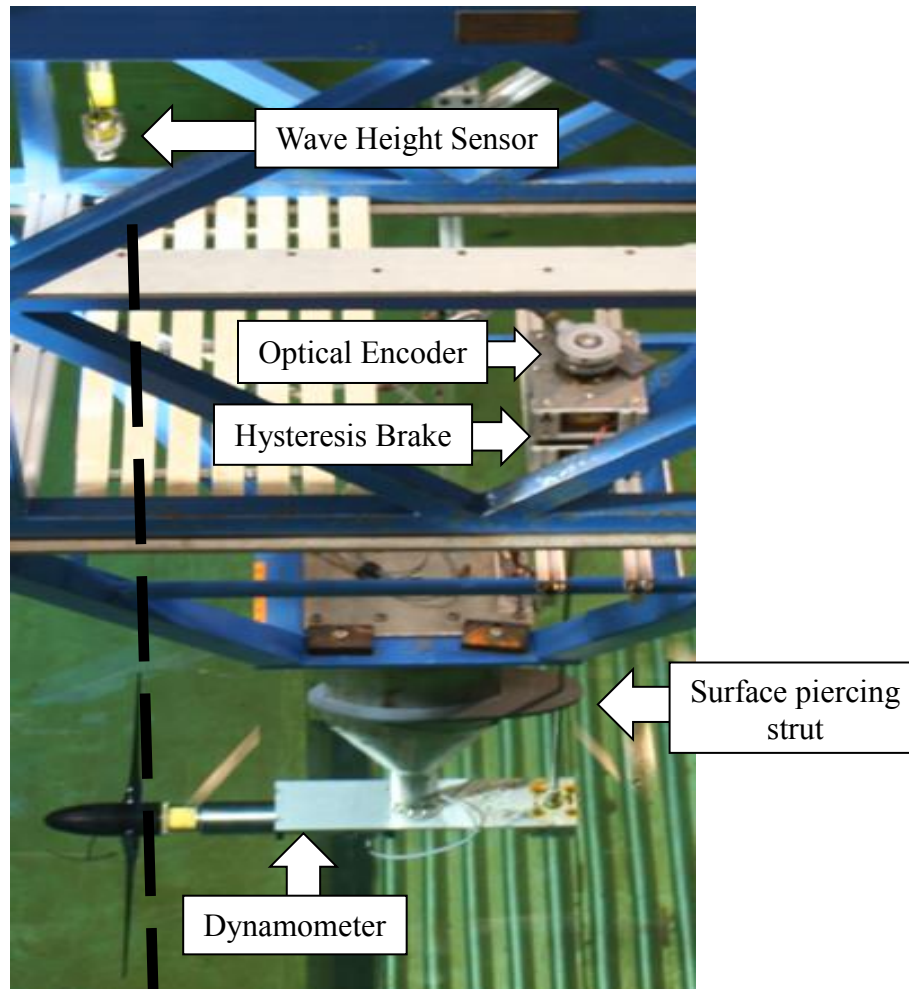
Figure 6: Experimental set-up. Flow is from left to right. The wave height sensor was located in the turbine rotor plane. The accelerometers are not pictured here, but were placed on top of the strut.

PARAMETERS	UNITS	INSTRUMENT
Carriage Speed	m/s	Optical encoder (installed in tow tank facility)
Thrust	N	Cussons Technology R46-01 Propulsion Dynamometer
Torque	N-m	Cussons Technology R46-01 Propulsion Dynamometer
Rotational Speed	rev/s	BEI Sensors H25 incremental optical encoder
Reference Blade Position		BEI Sensors H25 incremental optical encoder
Wave Height	m	Senix Optical Wave Height Sensors
Acceleration	m/s^2	3 Sherborne Single-Axis Accelerometers
Fluid velocity	m/s	2 Nortek Vectrino+ Acoustic Doppler Velocimeters (ADV)

Table 1: Velocity and turbulence measurement instrumentation

Two Nortek Vectrino+ Acoustic Doppler Velocimeters (ADVs) were used to measure fluid velocities. One ADV was positioned upstream and out of the turbine rotor plane to measure fluid velocity in a flow field unaffected by the turbine. The other ADV was used to measure velocities in the near wake regions of the turbine. The ADVs measured fluid velocity in three dimensions within a sample volume of 2.57×10^{-7} m^3 by sending out an acoustical signal that was reflected by particles in the water occupying the sample volume [17]. The ADV internal software calculated the phase shift in an acoustic pulse to determine the average velocity in the sample volume in three components. During the wake survey tests, the tank was seeded with fine particles before each run to provide scattering particles for the ADV measurements. The ADV assembly for the near wake study is pictured in Figure 7. The near wake region included the area within one diameter downstream from the turbine.
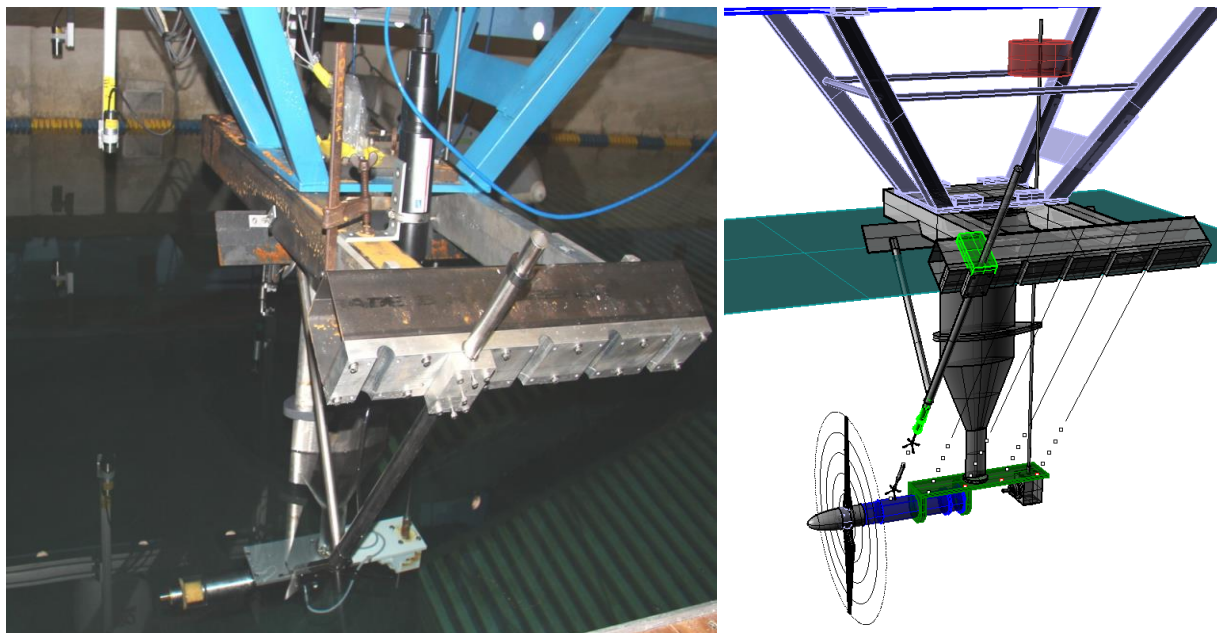

Figure 7: Arrangement of the ADV point measurement instrumentation. Two upstream ADV's are shown with their sample volumes (right). Carriage velocity is from right to left. Note five downstream locations behind the rotor plane for ADV placement. Second wave height sensor can be seen in the top left corner of the picture (left)

All instrumentation was synchronized to start data collection at the same time, and sampled at 700 Hz, with the exception of ADV's which sampled at the instrument maximum rate of 200Hz. Data collection was initiated by the operator on the carriage using MATLAB code. The majority of data runs, excluding tip speed ratio extrema at 5.5 and 11, were conducted at a constant carriage speed of 1.68 m/s, and data collection lasted 45 to 50 seconds, resulting in 30 to 35 seconds of steady state carriage travel down the tank. During two months of experiments in August and September 2013 more than 200 data sets were collected. A breakdown of the experimental matrix is given in Table 2.

		0.8D Tip Immersion	1.8D Tip Immersion
Performance Characteristics	Steady Flow	27	31
	Wave I (0.18m wave height)	9	10
	Wave I (0.09m wave height)	5	9
Near Wake Survey	Steady Flow	54	0
	Wave I (0.18m wave height)	6	0
	Wave II (0.09m wave height)	6	0

Table 2: Number of successful runs used for analysis under each condition

D. Summary of Wave Scaling

The first task of the Trident project was to conduct a literature search on wave theories, and scaling arguments for model testing [11]. Waves were expected to influence the performance characteristics of the model tidal turbine. Waves result in a streamwise velocity component, u_w, and a vertical velocity component, w_w, of the water particles that vary with the passing of the wave. The particle velocity induced by the wave decreases with increasing depth from the free surface, with magnitudes of zero at the bottom as a result of the no slip condition at the bottom boundary. The streamwise particle velocity, u_w, reaches a maximum in the direction of wave propagation at the wave peak and a maximum opposite the direction of wave propagation at the wave trough. The vertical particle velocity, w_w, has maximum upwards velocity at the upswell of the wave and maximum downwards velocity at the downswell of the wave.

The second order Stokes wave model was selected for wave modeling [11]. The second order Stokes wave is a progressive wave that moves forward over time imparting a net forward fluid particle velocity, called Stokes drift. The second order Stokes model predicts wave elevation using equation 8.

$$\eta = \frac{H}{2}\cos(kx - \sigma t) + \frac{H^2 k}{16}\frac{\cosh kh}{\sinh^3 kh}(2 + \cosh 2kh)\cos 2(kx - \sigma t) \qquad 8$$

Here, H is wave height, h is the mean water depth, x is the position dependent variable, and t is the time dependent variable. The wave number, k, is a function of the wavelength, λ, given by $2\pi/\lambda$. The angular frequency of the wave, σ, is a function of the wave period, P, given by $2\pi/P$.

The streamwise and vertical particle velocity components, u_w and w_w respectively, are predicted by the second order Stokes wave model by equations 9 and 10. The particle velocity components are a function of position, x, time, t, and depth, z.

$$u_w = \frac{H}{2}\frac{gk}{\sigma}\frac{\cosh k(h+z)}{\cosh kh}\cos(kx - \sigma t) + \frac{3}{16}\frac{H^2\sigma k \cosh 2k(h+z)}{\sinh^4 kh}\cos 2(kx - \sigma t) \qquad 9$$

$$w_w = \frac{H}{2}\frac{gk}{\sigma}\frac{\sinh k(h+z)}{\cosh kh}\sin(kx - \sigma t) + \frac{3}{16}\frac{H^2\sigma k \sinh 2k(h+z)}{\sinh^4 kh}\sin 2(kx - \sigma t) \qquad 10$$

Stokes drift is caused by the term $2(kx - \sigma t)$, which increases streamwise velocity at the wave peak and decreases the streamwise velocity at the wave trough [11].

The experimental design required modeling realistic flow patterns experienced by tidal turbines in the field. The experiment required scaling wave parameters such that the wave induced velocity profile over the turbine rotor was similar to the wave velocity profile over the prototype turbine. Tidal turbines are typically installed in relatively shallow water, approximately 30 to 50 m deep [7]. A regular wave with wavelength of 90 m and a period of 8 seconds were selected as a representative wave. These wave parameters correspond to swell wave conditions typically found on the US eastern seaboard continental shelf [10]. The water depth, h, for these conditions was projected at 50 m and 100 m. The wave height scaling was based on a nominal wave steepness of $H/\lambda = 0.02$, and the two relative depths, h/λ.

Waves were classified based on the relative depth, defined as a ratio of water depth, h, to wavelength, λ. If the relative depth was greater than 0.5, the wave was classified as a deep water wave. If the relative depth was between 0.05 and 0.5, the wave is an intermediate water wave. If the relative depth is less than 0.05, the wave is a shallow water wave [11].

Parameters for the two waves selected for experimentation, based on steepness and relative depth scaling, are summarized in Table 3. The relative depths were 0.6 and 1.2 representing borderline intermediate-to-deep wave limit and purely deep wave, respectively. For the remainder of the report, the waves are referenced by their respective wave heights: 0.18 m and 0.09 m. Figure 8 depicts the relative position of the model turbine in the wave velocity fields for the selected waves. Normalized wave velocity profiles were determined for streamwise, u_w/U, and vertical, w_w/U, components, where U is U_{tow}. The second-order Stokes wave model was used for modeling, as described in the preceding paragraph. The streamwise particle velocity was shown at the peak and trough of the wave, corresponding to the largest magnitude of wave influence in the direction of wave propagation and opposite the direction of wave propagation, respectively. The vertical particle velocity was shown at the upswell and downswell of the wave, corresponding to the largest magnitude of wave influence in the positive and negative directions, respectively. The wave velocities in the turbine plane ranged from 5% to 10% of the tow velocity and increased closer to the free surface. The wave velocity shear was calculated as the change in u_w and w_w over the rotor diameter, the vertical coordinate. The wave velocity shear was largest for the 0.18m wave at 0.8D tip immersion depth. Decreasing the wave height and increasing the immersion depth resulted in lower wave velocity shear Table 3 displays the wave velocity shear predicted by the second order Stokes model.

	Wave Period P	Wave Height H	Wavelength λ	Steepness H / λ	Relative Depth h / λ
Wave I	2.3 s	0.18 m	8.25 m	0.022	0.6
Wave II	1.6 s	0.09 m	3.99 m	0.022	1.2

Table 3: Waves selected for experimental simulation of operating conditions. During experiments water depth in the large towing tank of the Hydromechanics Laboratory was h = 4.9m.

Tip Immersion Depth	0.18m Wave		0.09m Wave	
	$\dfrac{\delta u_w}{\delta z}\left[\dfrac{1}{s}\right]$	$\dfrac{\delta w_w}{\delta z}\left[\dfrac{1}{s}\right]$	$\dfrac{\delta u_w}{\delta z}\left[\dfrac{1}{s}\right]$	$\dfrac{\delta w_w}{\delta z}\left[\dfrac{1}{s}\right]$
0.8D	85.2×10^{-3}	85.8×10^{-3}	56.9×10^{-3}	56.9×10^{-3}
1.8D	46.1×10^{-3}	47.1×10^{-3}	20.9×10^{-3}	20.9×10^{-3}

Table 4: Wave velocity shear over the turbine diameter presented for all wave and tip immersion depth combinations. The largest shear was observed at 0.8D tip immersion under the 0.18m waves.
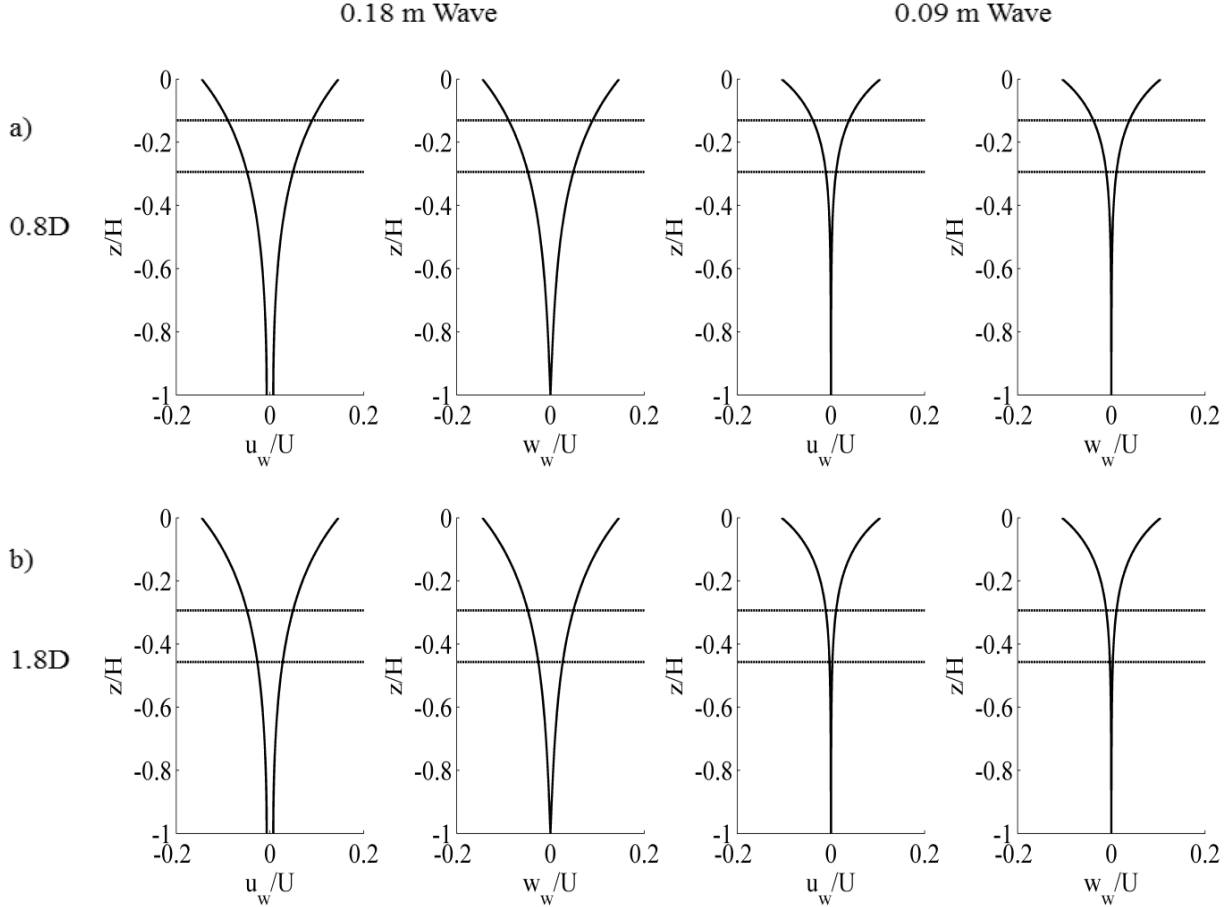

Figure 8: Wave velocity profiles determined using the second order Stokes wave model. Both waves used in experimentation are pictured. Horizontal lines represent the location of the turbine for a) 0.8D tip immersion and b) 1.8D tip immersion.

E. Cavitation Considerations

The cavitation number at the turbine tip was considered for the range of TSR measured. Cavitation is the formation of the vapor phase of water as a result of decreased local pressure. Cavitation was a concern on the low pressure side of the turbine blades (see Figure 3). The cavitation number is defined in equation 11. U_{rel} is given by equation 12.

$$\sigma = \frac{P_s - P_v}{\frac{1}{2}\rho U_{rel}^2}$$

11

$$U_{rel}^2 = U_{tow}^2 + (\omega R)^2 \qquad\qquad 12$$

P_s is the local pressure at the turbine rotor tip depth, a combination of dynamic and static pressures, and P_v is the vapor pressure at the water temperature.

The ambient pressure was assumed to be atmospheric. The water temperature was monitored throughout the experiment and remained constant at 20°C. Figure 9 shows the cavitation number over the measured TSR range for the two tip immersion depths. The transition from positive to negative σ indicated that cavitation may occur at TSR > 8.6. At higher TSR, several runs indicated an increased cavitation number, diverging from the observed pattern for the TSR range from 7 to 10. The increase resulted from higher tow speeds required to achieve the higher TSR. Under waves, the cavitation number transition occurred sooner as the trough of the wave reduced the tip immersion depth from the free surface, reducing local static pressure.
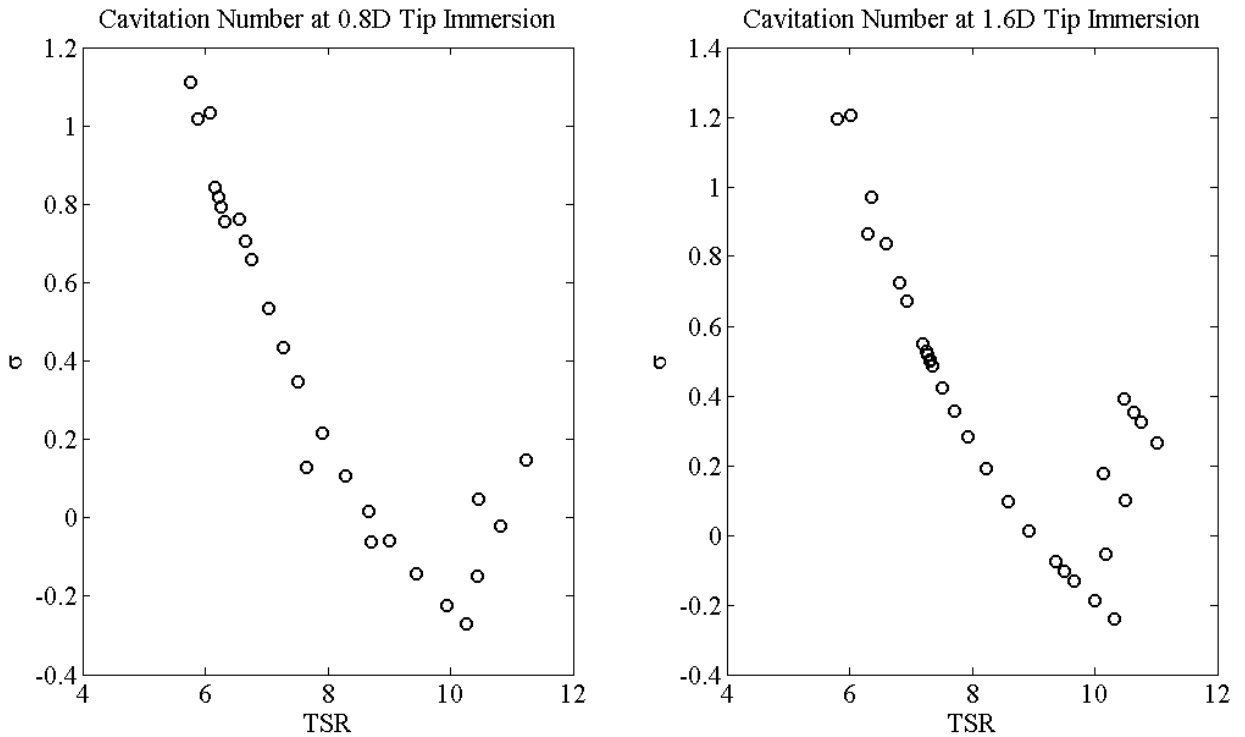

Figure 9: Cavitation number for TSR range tested. The transition to negative σ indicated cavitation occurs at TSR > 8.6. Cavitation was not expected in the range of TSR corresponding to maximum power coefficient, Cp.

F. Conditional Sampling Based on Reference Turbine Position

Throughout the analysis, measured quantities were conditionally sampled based on the turbine position, using the time history of the location of the reference blade, given by the Z-pulse. The method for conditional sampling utilized the Z-pulse and the assumption that rotational speed was constant between pulses. The Z-pulse operated by sending an analog 5 volt signal each time the optical encoder was activated by the spinning turbine. The Z-pulse signal was initiated when the reference turbine blade was at the top dead center position, perpendicular to the water surface, indicated in Figure 10. The angular position of the turbine, θ, was defined from this reference position. The turbine blades rotated in a clockwise direction when viewed upstream from the turbine. Figure 10 demonstrates this notation for θ = 90°. The colored blade represents the reference turbine

blade. The angular position of the turbine was given in degrees measured clockwise from the top dead center position.
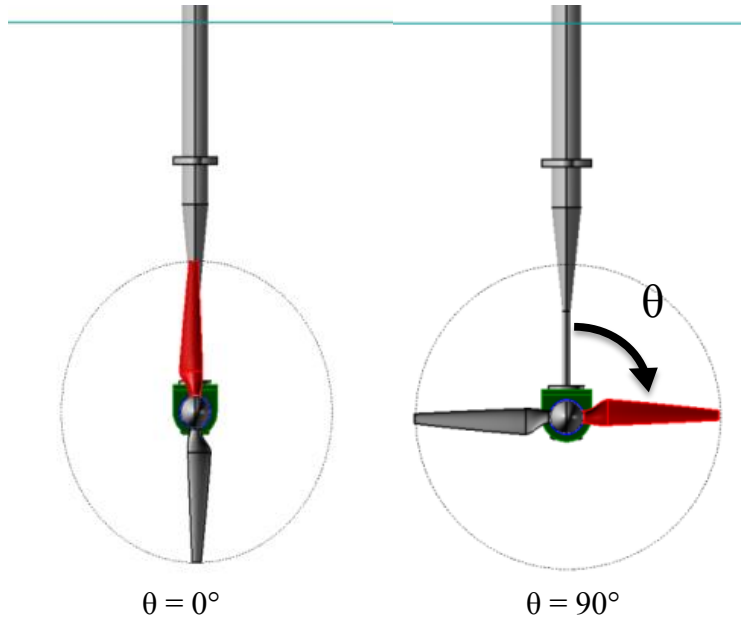

$\theta = 0°$ $\theta = 90°$

Figure 10: Notation for the angular position of the turbine reference blade. Top dead center position, $\theta = 0°$, is shown on the left. Turbine rotation is clockwise as seen from upstream. $\theta = 90°$ is pictured on the right.

A method was developed to estimate the time instances for any angular position of the turbine. The times at which the reference turbine blade was in the top dead center position, $\theta = 0$, were located using the leading edge of the 5V signal from the Z-pulse. Figure 11(b) demonstrates the acquisition of these instances, denoted by the 'x' at the leading edge of each Z-pulse. Other blade angular positions were interpolated using the time between two consecutive Z-pulse leading edges, equivalent to one full revolution of the reference blade. The interpolation was permissible when shaft rotational speed, ω, was constant throughout the revolution, as in Figure 11(a).

The time between consecutive Z-pulse leading edges was divided into the desired number of sections using $360°/m$, where m was the interval between samples, in degrees. The degree spacing was selected based on the rotational speed of the turbine. An interval of $90°$ was used for conditional sampling of performance characteristics. A different interval was selected for the near wake survey. At the rotational speed selected for the near wake survey, the turbine spun $2.5°$ for each sample taken by the optical encoder at 700 Hz. To tighten the interval without losing accuracy, m was set at $10°$. The $10°$ division between Z-pulse signals is demonstrated in Figure 11(b). As a result of the division, a time index was obtained at $10°$ intervals of the turbine blade rotation for wake measurements. Figure 11(c) demonstrates the conditional sampling method as performed on the ADV's measured axial fluid velocity, u_z, in the near wake based on turbine angular position of $\theta = 90°$.

In order to conditionally sample the fluid velocity in the wake, the time scale from the Z-pulse, sampling at 700 Hz, was converted to the time scale from the ADV sensor, sampling at 200 Hz. The measurements for corresponding time instances were found, as demonstrated by the boxes and arrows in Figure 11 (b) and (c). Once this was accomplished, the conditionally sampled measurements, denoted $\langle u_{inst.} \rangle_\theta$, were averaged for the entire run. Therefore, each quantity inside

angle brackets $< >_\theta$ used in the subsequent figures is an average value of a certain number of turbine cycles conditionally sampled based on the turbine angular position.
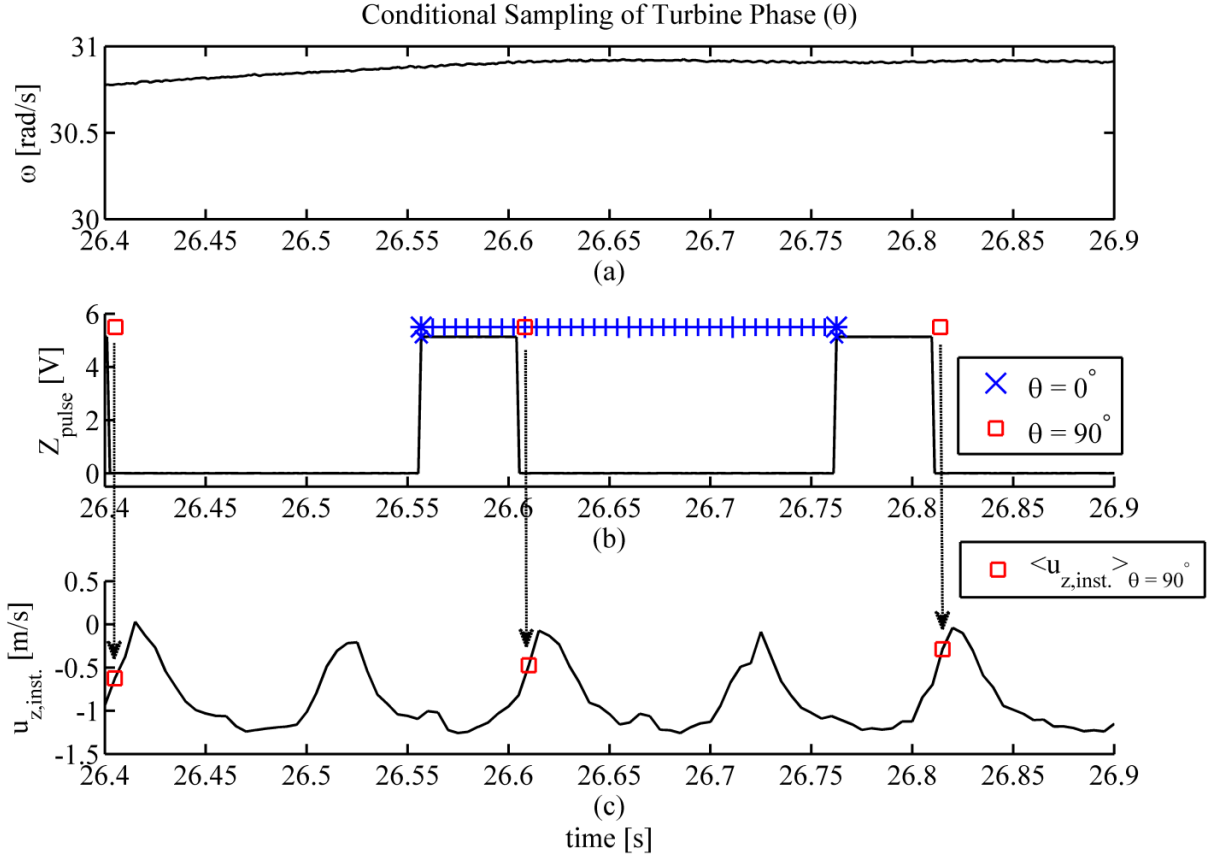

Figure 11: Conditional Sampling based on turbine angular position: a) variation of turbine rotational speed, b) time history of Z- pulse, and c) time history of ADV measured axial velocity. In all three plots, the horizontal axis indicates common time.

III.   Results

A. Baseline Steady Flow Conditions

Average power and thrust coefficients, C_P and C_T, respectively, for two tip immersions are plotted as a function of tip speed ratio, TSR, in Figure 12. Each point on the graph denotes one data run.   TSR during experimentation ranged from 5.5 to 11.5.   At TSR lower than 5.5, the hydrodynamic forces created by water flowing around the turbine blades did not overcome the torque from the brake. At TSR values higher than 11.5, the thrust generated approached thrust limits on the dynamometer. Consequently, experimental runs at TSR larger than 11.5 were not performed.

Since the turbine was tested in a tow tank not the open ocean, some of the fluid that would normally flow around the turbine rotor cross section was forced through the cross section. As a result, C_P, C_T, and TSR in the tow tank were larger than they would be in the open ocean. Therefore, a blockage correction was required to correct the measured data.   The correction factor was calculated a function of tow speed, thrust coefficient, tow tank parameters, and turbine parameters. The TSR correction was a ratio of the tow speed to the velocity required in the open ocean to induce the tow speed over the turbine. The C_P correction was the same ratio cubed due to the relationship

between C_P and U_{tow}. The C_T correction was the ratio from the TSR correction squared due to the relationship between C_T and U_{tow}. The correction factors ranged from 0.97 to 0.99 for TSR, 0.92 to 0.98 for C_P, and 0.95 to 0.99 for C_T [15].

The experimental uncertainty was determined to be 1% for TSR, C_P, and C_T [18]. The uncertainty was identified in all figures as a vertical error bar for C_P and C_T and a horizontal error bar for TSR. Uncertainty was displayed for one point in the maximum performance range of the turbine performance curve, as horizontal and vertical error bars.

The performance curves indicated a maximum C_P at TSR ≈ 6.2. At TSR lower than 6.2, much of the flow passing through the turbine blade rotor plane was not influenced by the turbine blades. Therefore, only a fraction of the available energy from the water was collected by the turbine. As the TSR was increased to 6.2, more energy was captured as the blades spun faster. When the turbine rotational speed was increased beyond 6.2, the blades forced more fluid around the turbine cross section, decreasing the energy extracted from the water. Additionally, less torque was developed by the turbine, further reducing the power developed. C_T increased with TSR. More water was forced around the cross sectional area at higher TSR, resulting in higher thrust on the turbine due to the conservation of momentum.

As shown in Figure 12, turbine immersion depth did not significantly affect the average C_P and C_T generated by the model turbine. In field applications of tidal turbines, the current velocity profile is dependent on depth due to the boundary layer on the ocean floor. For the experimental procedure, the simulated current velocity profile did not vary with turbine immersion depth because the observed water velocity at the top of the turbine and at the bottom of the turbine was equivalent to U_{tow}. The only change in the experimental parameters with depth was the local pressure increase as a result of the increased depth. The pressure difference was on the order of 6 kPa, 5.7% of the static pressure at the turbine center with 0.8D tip immersion depth.
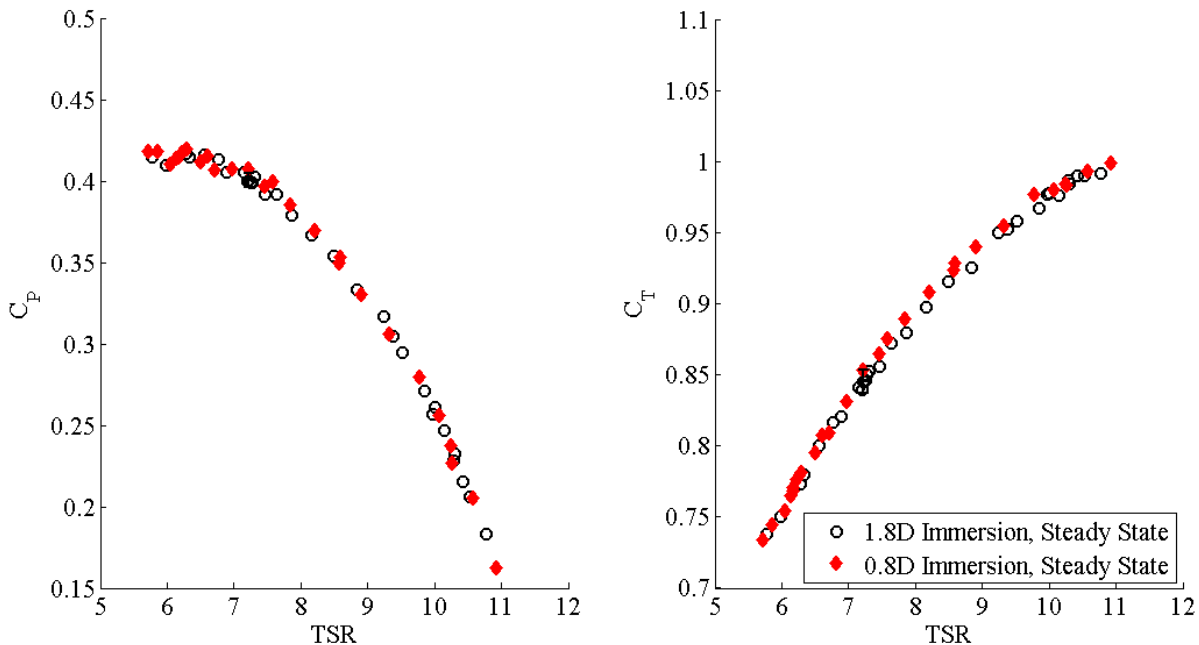

Figure 12: Influence of tip immersion depth on C_P and C_T under steady flow. Optimal performance (maximum C_p) is achieved at TSR ~ 6.2. Immersion depth does not affect turbine performance.

B. Conditional Sampling Based on Reference Blade for Steady Flow Conditions

In order to determine the influence of turbine blade position on turbine performance without waves, torque, thrust, and rotational speed time histories were conditionally sampled based on the reference blade position using the procedure described in the previous section. Figure 13 displays the conditionally sampled power and thrust coefficients at 0.8D tip immersion. For the power coefficient each point represents $<C_P>_\theta$ magnitude at one angular position of the turbine averaged for the entire run. Results indicate that conditionally averaged C_P was not affected by turbine angular position for the steady inflow condition.

Turbine position may have influenced C_T. $<C_T>_\theta$ experienced increased variability at TSR > 8.6. Also, $<C_T>_\theta$ was consistently larger at $\theta = 90°$ and consistently smaller at $\theta = 270°$ for this TSR range and the variations are larger than the experimental uncertainty. The variation noticeably begins at the same TSR for which cavitation may occur. Cavitation was more likely to occur at shallower immersion depths because of the decrease in static pressure. For $\theta = 0°$ and $180°$, one blade experienced lower pressure than the other. $<C_T>_\theta$ for these positions was very close in magnitude to the mean value for the entire run. For $\theta = 90°$ and $270°$, cavitation was possible on both blades. Cavitation tends to lower the thrust on a turbine. Therefore, the lowered $<C_T>_\theta$ at $\theta = 270°$ was explained by cavitation experienced on both blades at this turbine position. The increase in thrust observed at $\theta = 90°$ was not fully explained by cavitation.
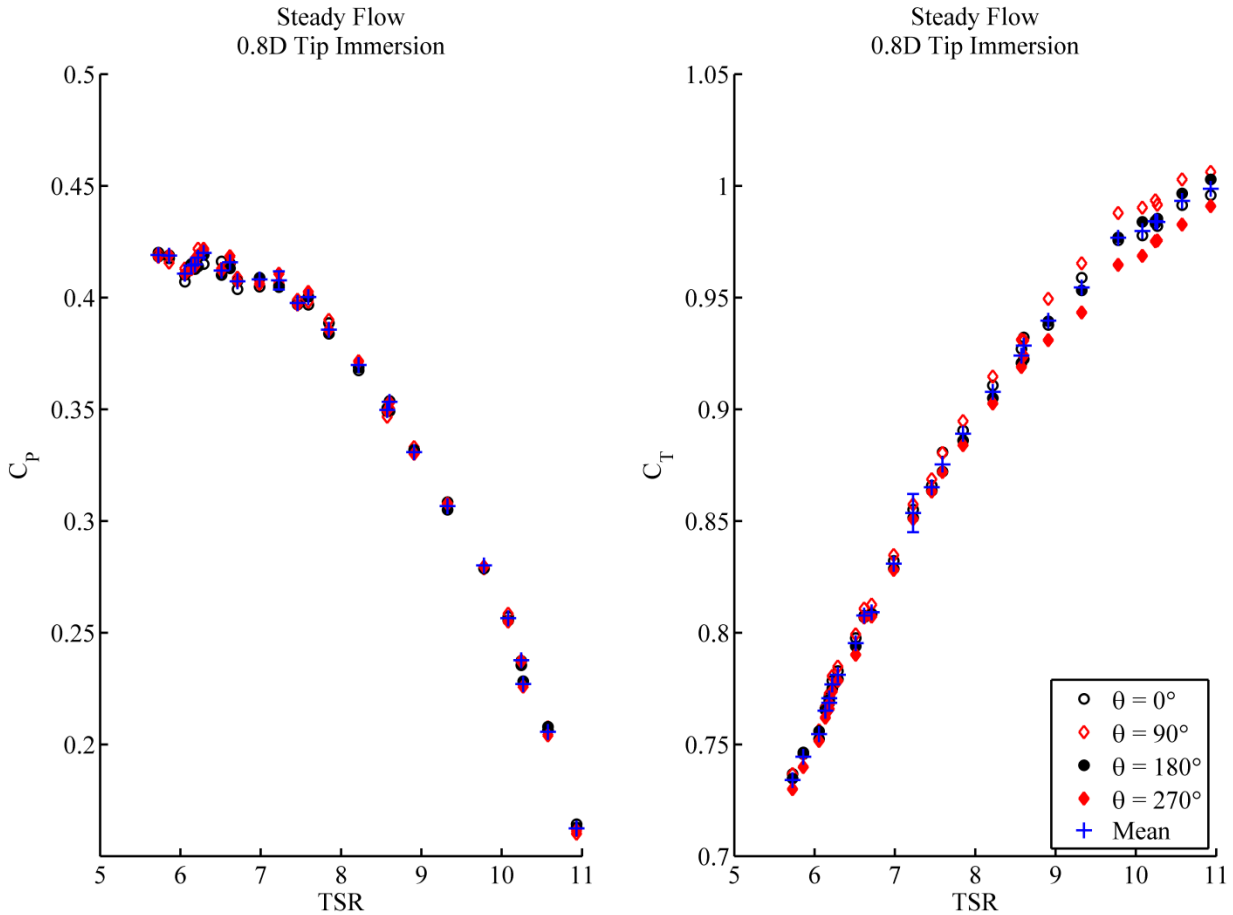

Figure 13: Influence of turbine angular position on conditionally sampled C_P and C_T at 0.8D tip immersion depth. No effect was observed in $<C_P>_\theta$. At $\theta=90°$, $<C_T>_\theta$ was consistently higher than other angles for TSRs ranging from 8.6 to 11. At $\theta=270°$, $<C_T>_\theta$ was lower for TSRs of 8.6 to 11.

The analysis at 0.8D tip immersion was repeated for 1.8D tip immersion tests in Figure 14. The power coefficient, $<C_P>_\theta$ demonstrated no dependence upon turbine blade position. Large variability was observed at low TSR as a result of resonance in the testing equipment. The longer shaft used to connect the brake to the turbine at the deeper immersion depth resonated when the turbine was heavily loaded. The resonance resulted in high variability of rotational speed, causing high variability in measured power. $<C_T>_\theta$ did not experience the same variability at low TSR.

Conditionally sampled, $<C_T>_\theta$ experienced increased variability at TSR > 8.6. The dependence of $<C_T>_\theta$ on turbine blade position observed at 0.8D immersion for certain TSR was repeated at 1.8D immersion, but for different angles. $<C_T>_\theta$ was consistently larger at $\theta = 0°$ and smaller at $\theta = 180°$ for TSRs ranging from 8.6 to 11. Cavitation was less likely to occur at the increased immersion depth. It is possible that cavitation was not experienced on either blade at $\theta = 90°$ and $270°$. Cavitation would be more likely to occur on a single blade at $\theta = 0°$ or $180°$. This would explain lower $<C_T>_\theta$ at $\theta = 180°$. The increased $<C_T>_\theta$ at $\theta = 0°$ was not explained by cavitation.
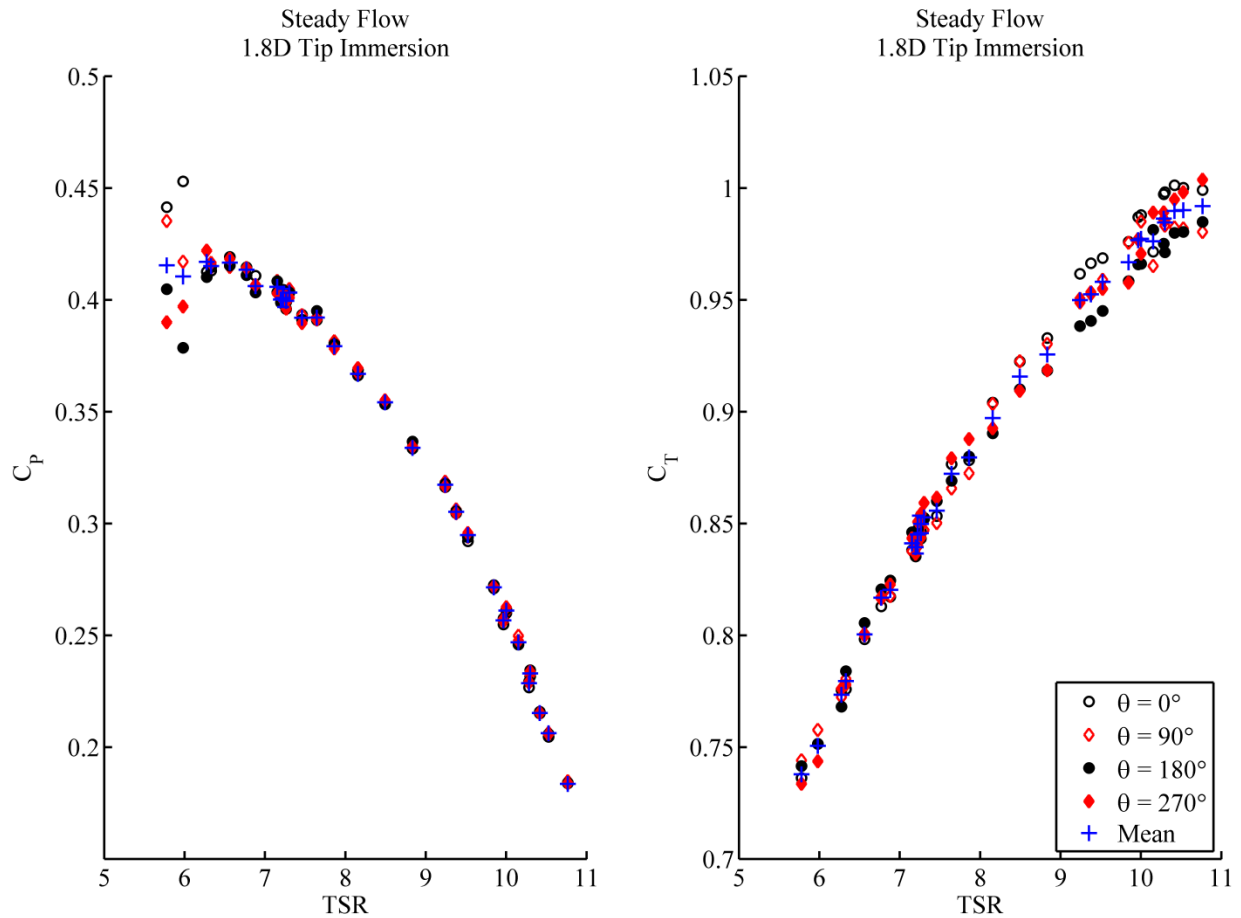

Figure 14: Influence of turbine angular position on conditionally sampled C_P and C_T at 1.8D tip immersion depth. No effect was observed in $<C_P>_\theta$. However, large variations were observed at low TSR, due to resonance in the experimental equipment. At $\theta=0°$, $<C_T>_\theta$ was consistently higher than other angles for TSRs ranging from 8.6 to 11. At $\theta=180°$, $<C_T>_\theta$ was lower for TSRs of 8.6 to 11.

C. Unsteady Flow Conditions

In order to quantify actual inflow wave conditions, wave data from a stationary wave capacitance probe placed in the in the towing tank during experiments was analyzed to confirm the second order

Stokes wave model as an accurate representation of the waves generated by the wave-maker. The Airy wave and the second order Stokes wave models were compared to the measured wave surface elevation time history from the capacitance probe located at mid-length of the towing tank during experiments with waves [11]. The Airy wave model wave elevation was given by equation 13. The second order Stokes prediction of wave elevation was given in equation 14.

$$\eta = \frac{H}{2}\cos(kx - \sigma t) \tag{13}$$

$$\eta = \frac{H}{2}\cos(kx - \sigma t) + \frac{H^2 k}{16}\frac{\cosh kh}{\sinh^3 kh}(2 + \cosh 2kh)\cos 2(kx - \sigma t) \tag{14}$$

Figure 15 demonstrates the conformity of the measured 0.18 m wave to the second order Stokes model. The Airy wave model was also plotted. The wave peak is located at $\phi = 0°$, and the wave trough is located at $\phi = \pm180°$, where ϕ is the instantaneous phase of the measured free surface elevation. The second order Stokes wave elevation was a better prediction of the measured incoming waves than the Airy wave model, with better predictions of wave elevation at the wave peak and trough. The slope of the 0.18 m wave was predicted accurately by the models.
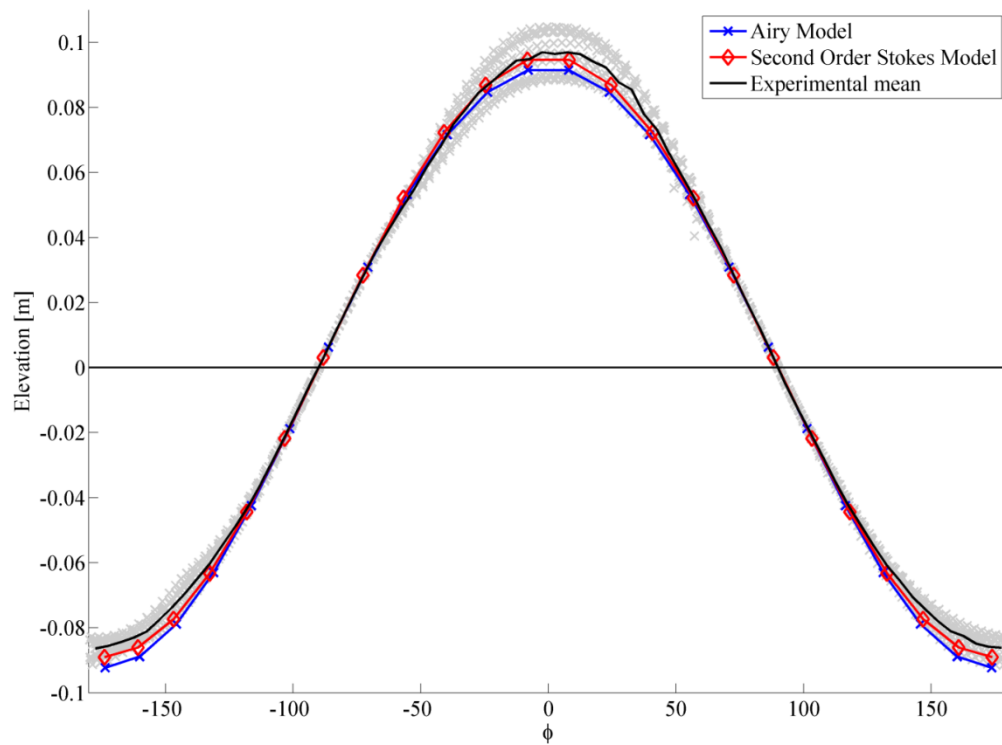

Figure 15: Conformity of measured wave elevation for the 0.18 m wave to the second order Stokes and Airy wave models. Second order Stokes provides a better approximation of the measured surface elevation. Gray data points indicate measured wave elevation, and horizontal line is the undisturbed free surface.

The 0.09m wave elevation was similarly predicted by the two models, as shown in Figure 16. Both wave models were good predictions of the generated waves in the towing tank. The second

order Stokes model wave proved slightly more accurate in predicting the actual (measured) wave peaks and troughs.
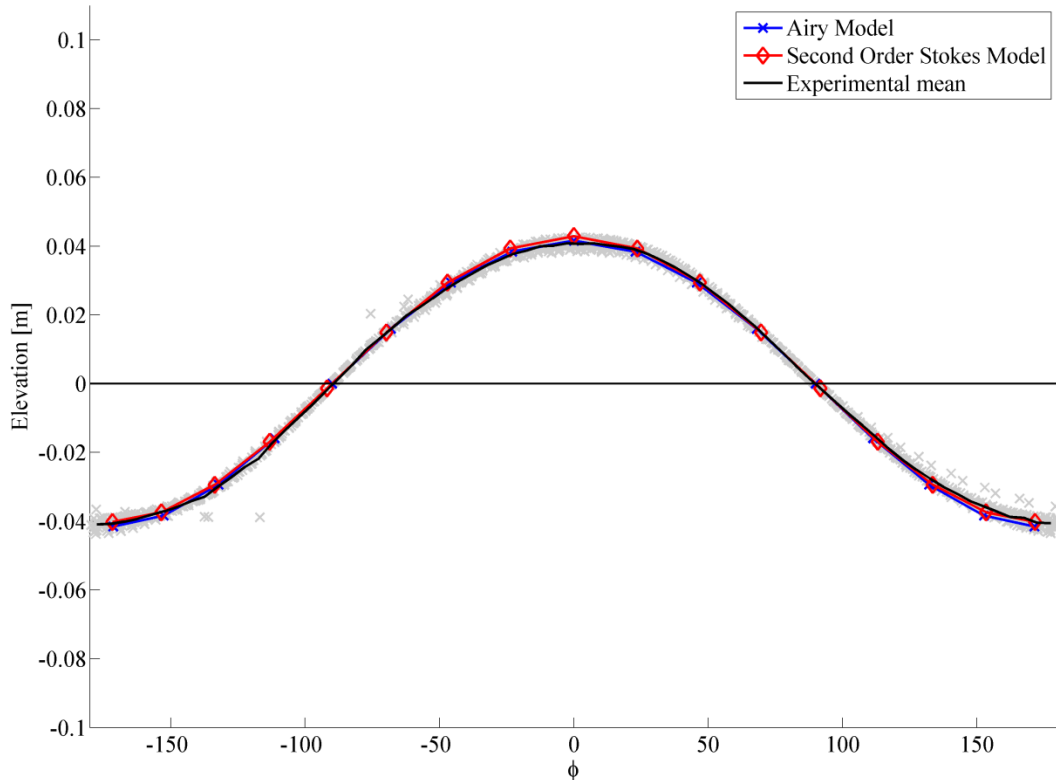

Figure 16: Conformity of wave elevation data for the 0.09m wave to second order Stokes and Airy wave models. Symbols are the same as in Figure 15.

D. Unsteady Flow Performance Characteristics

The effects of waves on the average coefficients of power, C_P, and thrust, C_T, were compared at 0.8D tip immersion depth in Figure 17. The tests conducted with waves exhibited slightly higher average power and thrust coefficient than those without waves. The increased net forward velocity of the water from the waves caused the increase. The 0.18m wave, imparting a larger net velocity increase, had higher C_P and C_T. The increase was slight, yet larger than the experimental error.

A similar plot for 1.8D tip immersion is shown in Figure 18. The increase in average power and thrust coefficient observed with waves was less apparent than at 0.8D immersion, indicating that waves have less influence on turbine performance at deeper immersion depths. The conclusion was consistent with the influence expected from lower wave velocities and shear at increased depth (Figure 8).

A possible explanation of the slight increase in C_P and C_T for 0.8D immersion depth was the Stokes drift of the progressive waves. Stokes drift is a phenomenon of progressive waves that results in a net forward velocity of a particle in the streamwise direction of wave propagation. The Stokes drift decreased with increased depth. The depth averaged Stokes drift velocity, over the rotor

diameter, was approximately 0.014 m/s [18]. Using the relationships between velocity and the performance characteristics described during the blockage correction explanation, Stokes drift was determined to increase C_P, C_T, and TSR by 3%, 2%, and 1% respectively, which accounts for the difference shown in Figure 17. A similar analysis was conducted for 1.8D tip immersion depth. The Stokes drift was approximately 0.003 m/s [18]. The resulting increase in C_P, C_T, and TSR was calculated as 0.5%, 0.5%, and no increase respectively. The predicted increases in C_P and C_T were observed in Figure 18 although the influence from Stokes drift was not much greater than the experimental uncertainty.
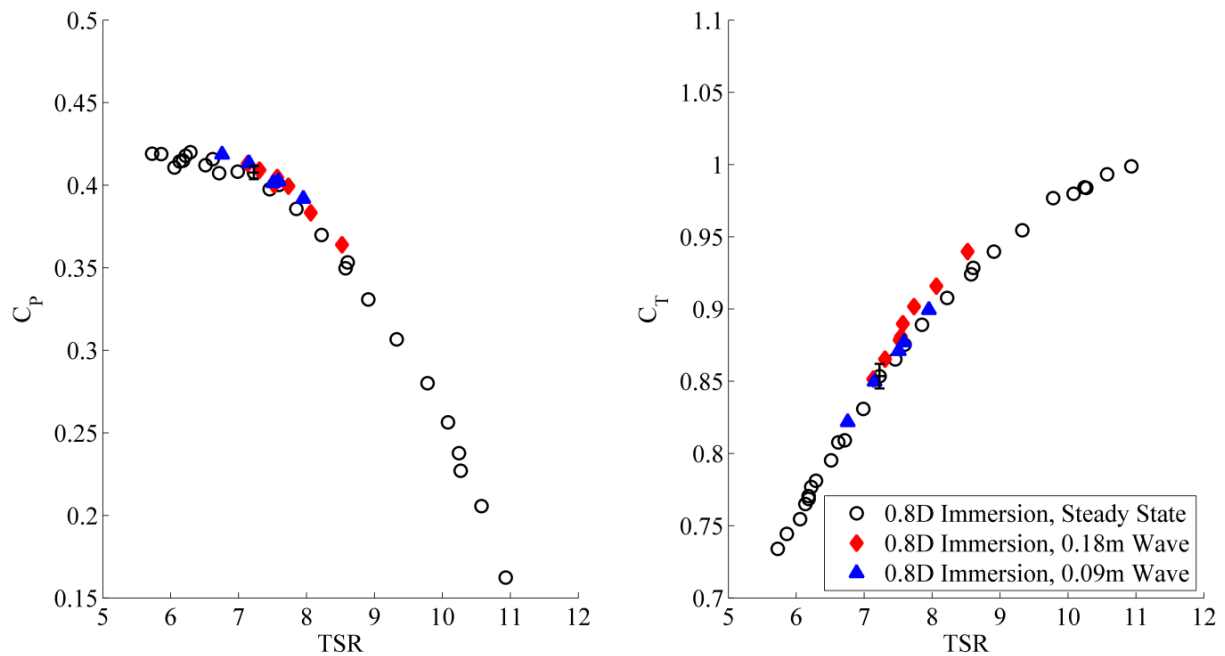

Figure 17: Influence of waves on C_P and C_T at 0.8D tip immersion depth. Both C_P and C_T demonstrated a slight increase with waves. The increase was larger for the 0.18 m wave than the 0.09 m wave. The increase was a result of a net increase in velocity from the waves known as the Stokes drift. Error bars demonstrate experimental uncertainty.
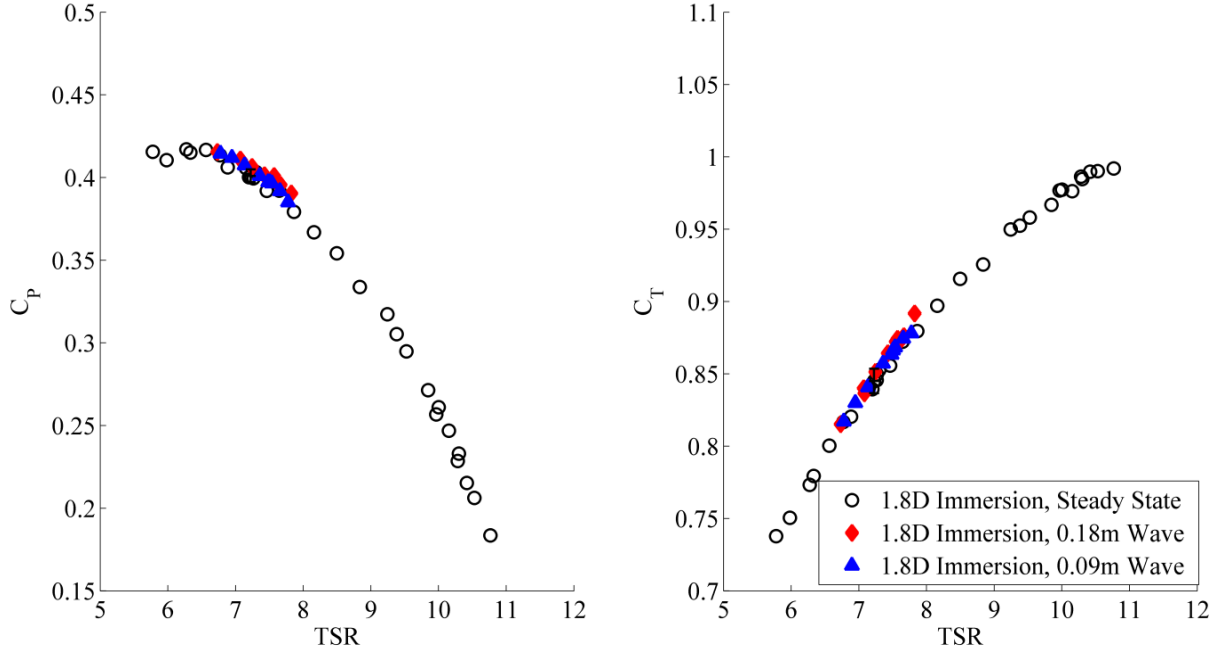
Figure 18: Influence of waves on C_P and C_T at 1.8D tip immersion depth. The increase in C_P and C_T was less significant than at 0.8D tip immersion.

E. Conditional Sampling based on Wave Peaks and Troughs

To further examine the effects of waves on turbine performance at 0.8D tip immersion, values of torque, thrust, and rotational speed (ω) were conditionally sampled at the peak and trough of the wave. A peak and trough average value was determined for each experimental run. Torque, thrust and ω were plotted instead of C_P and C_T in order to present a clearer picture of the wave influence. As a result, blockage corrections were not included in Figures 19 and 20. Figure 19 shows torque, thrust, and ω conditionally sampled based on the peaks and troughs of the 0.18 m and 0.09 m waves at 0.8D tip immersion. The 0.18 m waves had a larger influence than the 0.09 m waves because of higher velocity magnitudes as predicted in Figure 8. Torque values were nearly identical for both wave types at the peak and trough. These values were very close to the average for the entire run. The torque was inversely related to TSR because of the hydrodynamic characteristics of the turbine. Rotational speed, ω and TSR were directly proportional to one another because the turbine radius and carriage speed were constant for each experimental run. The instantaneous values of ω were shifted by the optical encoder. The values of ω were corrected to demonstrate a maximum at the wave peak and a minimum at the trough for both waves. This relationship was consistent with previous experiments [8, 9]. The 0.18m wave resulted in a larger influence on ω than the 0.09 m wave. The range from peak to trough of ω was constant at 8.5 rad/s for the 0.18 m wave and 1.6 rad/s for the 0.09 m wave. The influence of waves on ω was not dependent on TSR.

The thrust was highly dependent on the wave phase. Thrust reached a maximum at the wave peak, and a minimum at the wave trough. The 0.18 m wave resulted in higher thrust variation than the 0.09 m wave. The influence of waves on the thrust demonstrated dependence on TSR. The difference in thrust from wave peak to trough under 0.18m waves decreased from 64% to 49% of the average thrust for each run with increased TSR. The difference decreased from 26% to 20% for

0.09m waves. Waves had less influence on thrust at higher TSR. The effect of wave phase on turbine performance was dependent on the operating conditions.
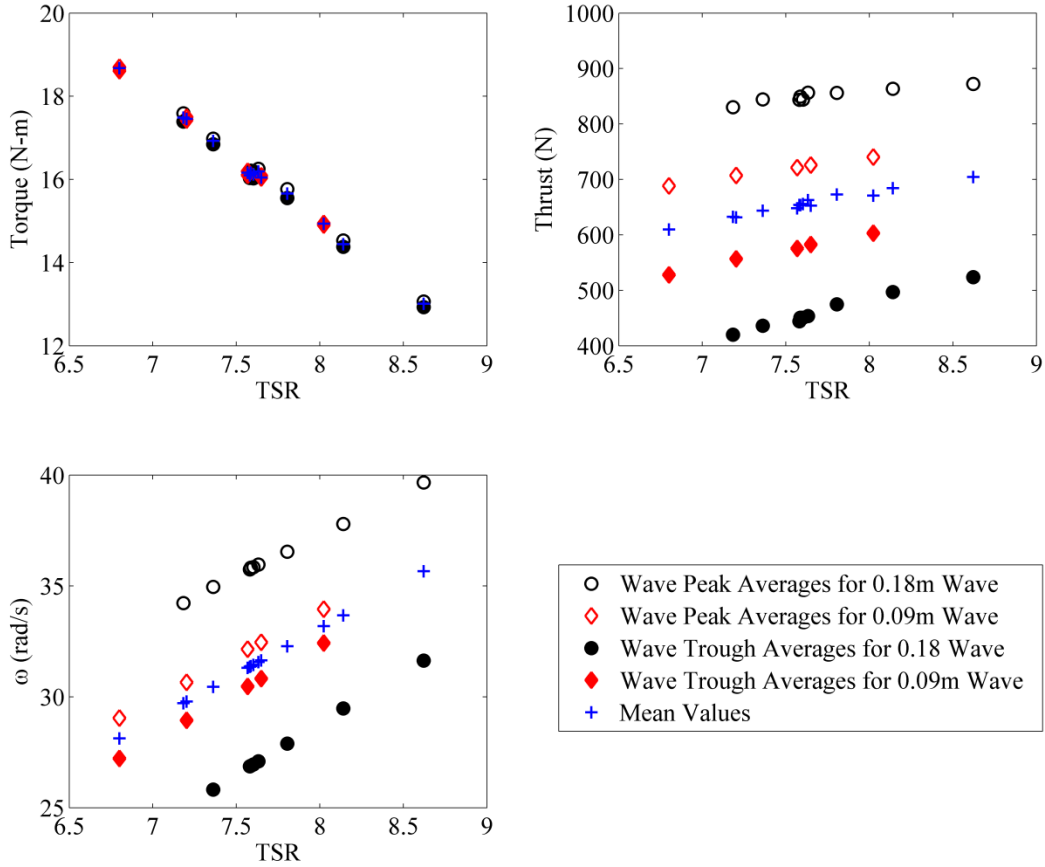

Figure 19: Influence of wave phase on turbine performance at 0.8D tip immersion depth. The torque was inversely proportional to TSR; ω was proportional to TSR. ω demonstrated dependence on wave phase. The time history of ω was shifted by the optical encoder. Values were corrected to demonstrate a maximum value at wave peak and a minimum at wave trough. Thrust demonstrated high dependence on wave phase. The dependence appeared to decrease at higher TSR.

The evaluation of the wave phase influence on turbine performance was repeated at 1.8D tip immersion depth. The relationships were identical, but the magnitudes were smaller as indicated in Figure 20. The decreased influence of both waves was a result of lower velocity magnitudes at the deeper immersion depth as predicted in Figure 8. The torque was not affected at the peak and trough of the waves. The rotational speed, ω, was shifted to demonstrate a maximum at the wave peak, and a minimum at the wave trough. The shift was necessitated by the recording delay of the optical encoder. The 0.18 m wave caused a 5 rad/s difference in ω from peak to trough, while the 0.09 m wave only caused a 0.5 rad/s difference in ω. The influence of waves on ω was not dependent on TSR. The thrust was largest during the wave peak, and smallest during the wave trough. These values were centered on the average thrust for the run. The influence of waves on thrust was dependent on TSR. For 0.18m waves, the thrust range from peak to trough decreased from 41% to

32% of the average thrust at higher TSR. The range decreased from 8% to 6% of the average thrust for 0.09m waves. The thrust variation experienced by the turbine was highly dependent on turbine immersion depth.
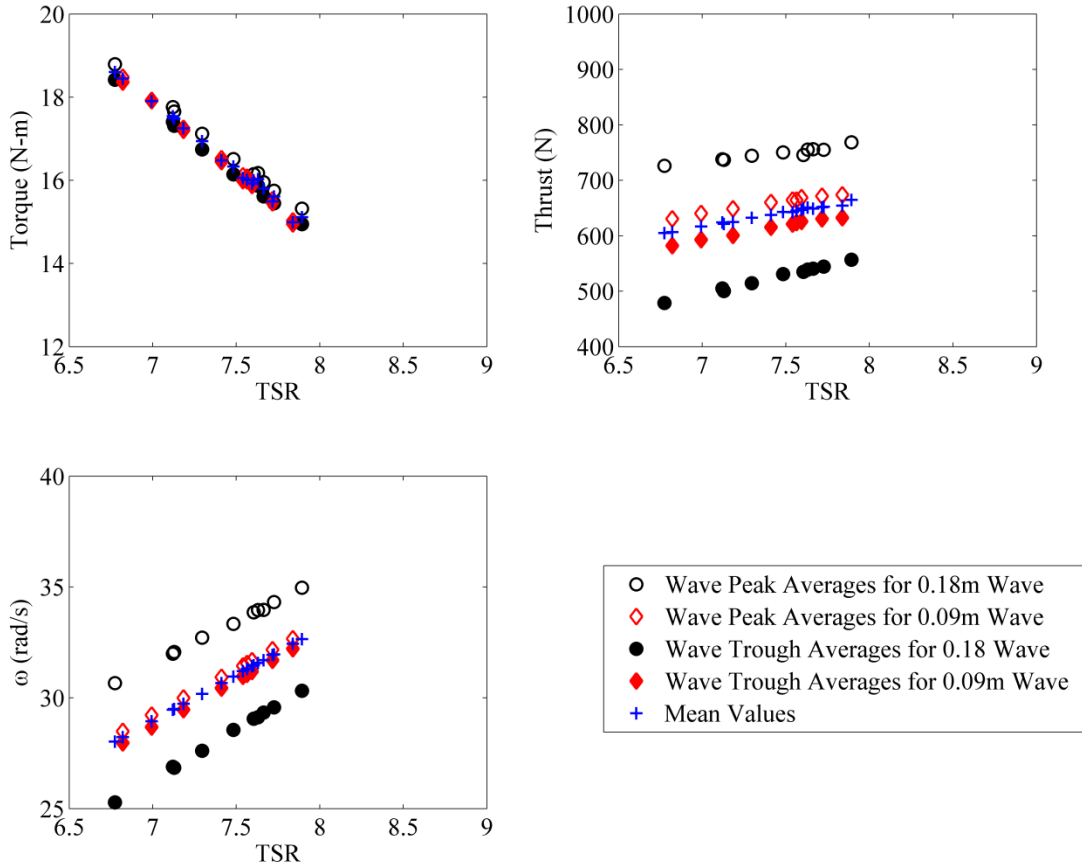

Figure 20: Influence of wave phase on turbine performance at 1.8D tip immersion depth. The behavior was similar to 0.8D immersion, but the magnitude of the influence was decreased.

F. Wave Phase Averaging

Figures 21 through 24 depict performance characteristics parameters conditionally sampled based on instantaneous wave phase, ϕ, for the 0.18 m and 0.09 m waves, at 0.8D and 1.8D tip immersion depth. Instantaneous wave phase was obtained using the Hilbert transform to convert the data from time to phase, using filtered data from the surface elevation time history [19, 20, 21]. In the figures, the wave trough is located at $\phi = +/-180°$ and the wave peak at $\phi = 0°$. The dashed horizontal line depicts the average value for the run, i.e. average over all wave phases. Data points are also shown in grey. The black solid line is the phase average for that quantity, determined using the average value of the quantity over five degree intervals.

In Figure 21, the top plot depicts the wave surface elevation, in meters, as a function of the wave phase. Nominal (input) wave height to the wave maker was set to 0.18 m for intermediate waves, and is consistent with the measured wave elevation. A Hilbert transformation was conducted on the surface elevation, or wave height, transforming it from time to phase [20]. The next plot beneath is

the shaft speed versus wave phase and indicates maximum value at the peak of the wave and the minimum at the wave trough, consistent with previous experiments [8, 9]. The rotational speed was influenced primarily by the streamwise velocity component of the wave. Higher instantaneous velocities resulted in larger ω. The shaft speed varied by 10 rad/s, 33% of the mean value of 30.5 rad/s. Initially, the shaft speed data were shifted by a 0.3 second delay. The delay was caused by optical encoder used to measure ω. The shaft speed in Figures 21 through 24 was shifted such that the maximum value occurred at the peak of the wave, and the minimum value occurred at the trough of the wave. Further consideration of the delay was conducted using the Z-pulse to verify ω. The Z-pulse indicated a maximum ω at the wave peak.

Torque demonstrated a high degree of variability. The range of torque values covered 6% of the overall mean value, 16.9N-m. While the range was not the largest observed for displayed parameters, the variability within the range was very large. The phase averaged mean value was 45° out of phase with the wave. The torque responded to the vertical and streamwise velocity components induced by the waves. The maximum value occurred when the vector sum of the two components was a maximum. The power coefficient was influenced strongly by ω. As a result, the power coefficient, C_P, was nearly in phase with the wave elevation. The small shift observed in Figure 21 was a result of influence from the torque. A maximum value of approximately 0.51 was achieved at the wave peak, and a minimum value of 0.35 occurred at the trough. The range was 37% of the overall mean value of 0.43. The thrust coefficient, C_T, had a maximum value of approximately 1.2 near the wave peak, and a minimum value of 0.6 near the wave trough. The range was 77% of the overall mean, 0.91. The thrust was strongly influenced by the streamwise component of wave velocity. Higher streamwise velocities resulted in higher thrust on the turbine. The thrust was also influenced by the vertical component of the wave velocity, indicated by the shift in Figure 21.

Instantaneous wave phase conditional sampling was repeated for 0.09m waves at 0.8D tip immersion depth in Figure 22. Similar behavior was observed for rotational speed, torque, C_P, and C_T over the wave phase, ϕ. The effects were smaller due to the decreased velocity magnitudes produced by the wave as predicted in Figure 8. ω varied by 8% of the mean. Torque varied by 6%. C_P varied by 13%. C_T varied by 32%. There was a significant decrease in the periodic behavior of the performance characteristics with the 0.09m wave at 0.8D tip immersion depth.

For 1.8D tip immersion depth, the influence of the 0.18m wave was significantly decreased from 0.8D tip immersion depth, as shown in Figure 23. The decrease was a result of reduced magnitudes of wave velocity at the increased immersion depth (Figure 8). C_P, C_T, and ω were still in phase with the wave elevation. The torque was 90° out of phase with the wave elevation. The rotational speed variation decreased from 33% to 18% of mean ω. The torque range remained the same at 6%. C_P decreased from 37% to 23%. C_T decreased from 77% to 43%. The reduced influence on the performance characteristics resulted from the smaller magnitude of wave velocity fluctuations in the flow and the reduced shear across the turbine blades (Figure 8).

The 0.09 m waves had very little influence on performance characteristics at 1.8D tip immersion (Figure 24). C_P, C_T, and ω were still in phase with the wave elevation. The torque was 90° out of phase. 1.8D tip immersion with 0.09m waves was predicted to have the least influence on turbine performance (Figure 8). A summary of the influence of wave phase on TSR, ω, Q, C_P, and C_T for each condition are tabulated in Table 5.
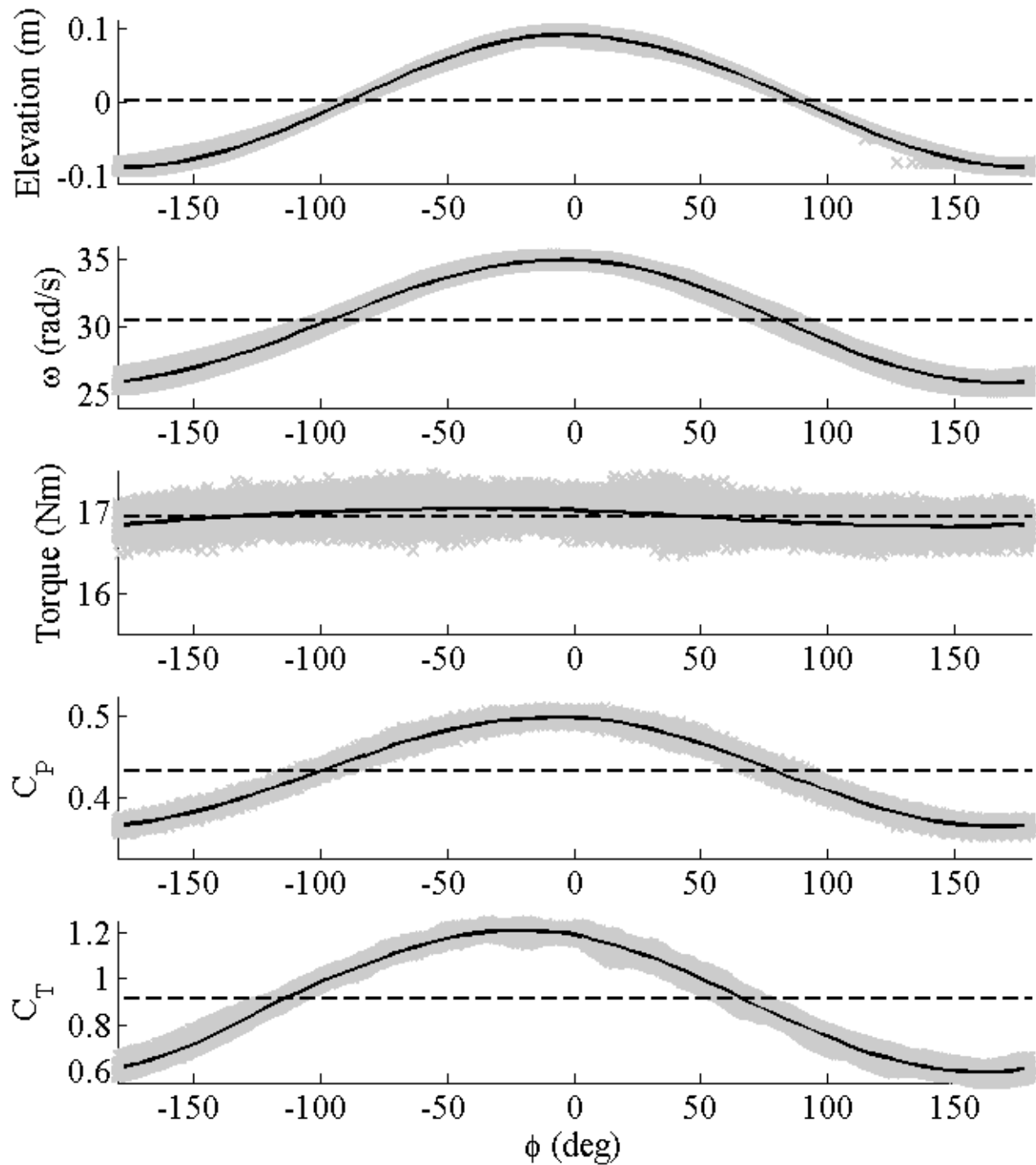
Figure 21: Turbine performance as a function of 0.18 m wave phase at 0.8D tip immersion. Shaft speed, ω, C$_P$, and C$_T$ varied in phase with wave surface elevation. Torque varied 90° out of phase with the surface elevation of the wave. 0.18 m waves had a significant effect on turbine performance over the wave phase at 0.8D tip immersion depth. Quantities determined at TSR = 7.25.
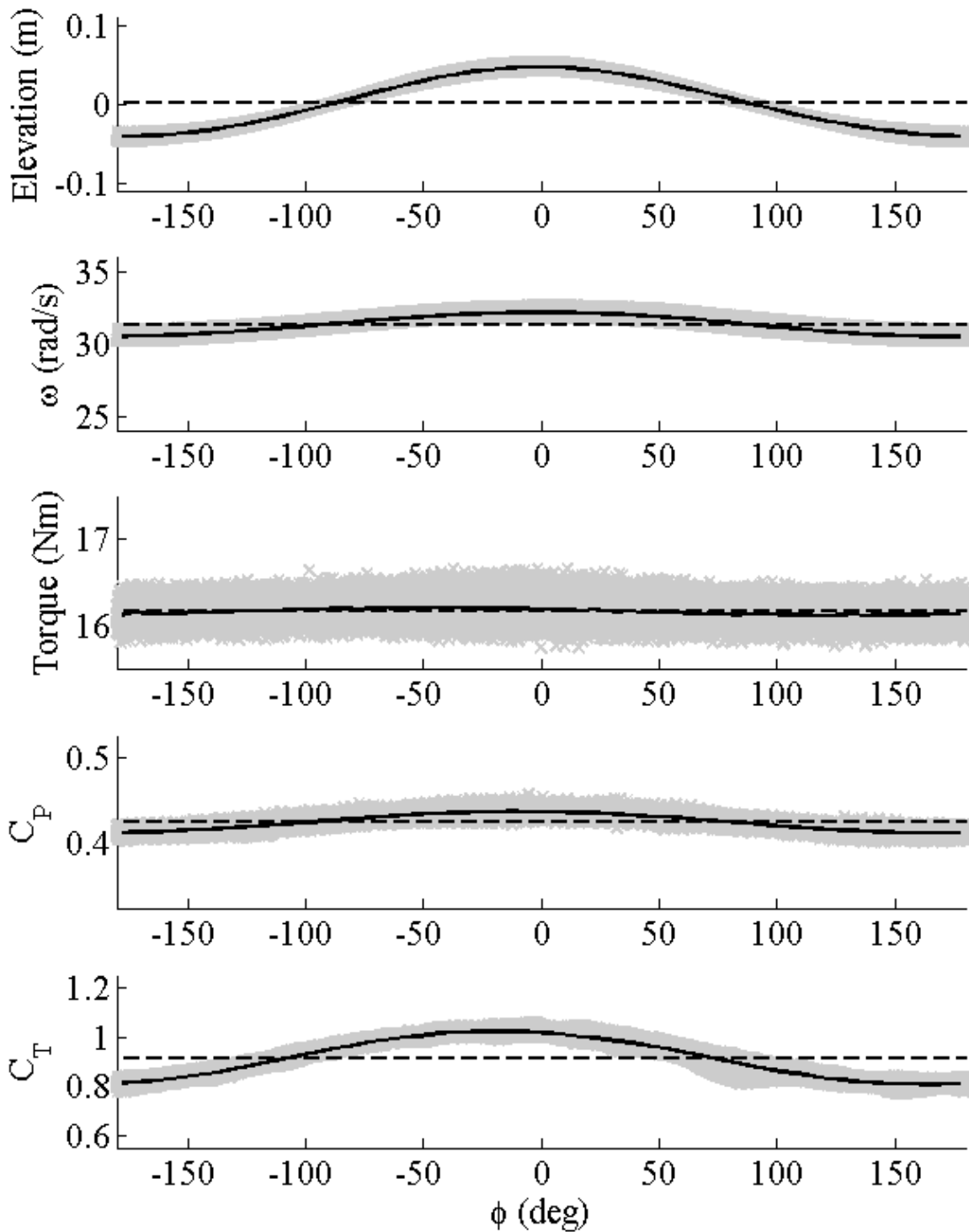
Figure 22: Turbine Performance as a function of 0.09 m wave phase at 0.8D tip immersion. Shaft speed, ω, C_P, and C_T varied in phase with wave surface elevation. Torque varied 90° out of phase with the surface elevation of the wave. 0.09 m waves had a decreased effect over the wave phase on turbine performance at 0.8D tip immersion depth. Quantities determined at TSR = 7.45.
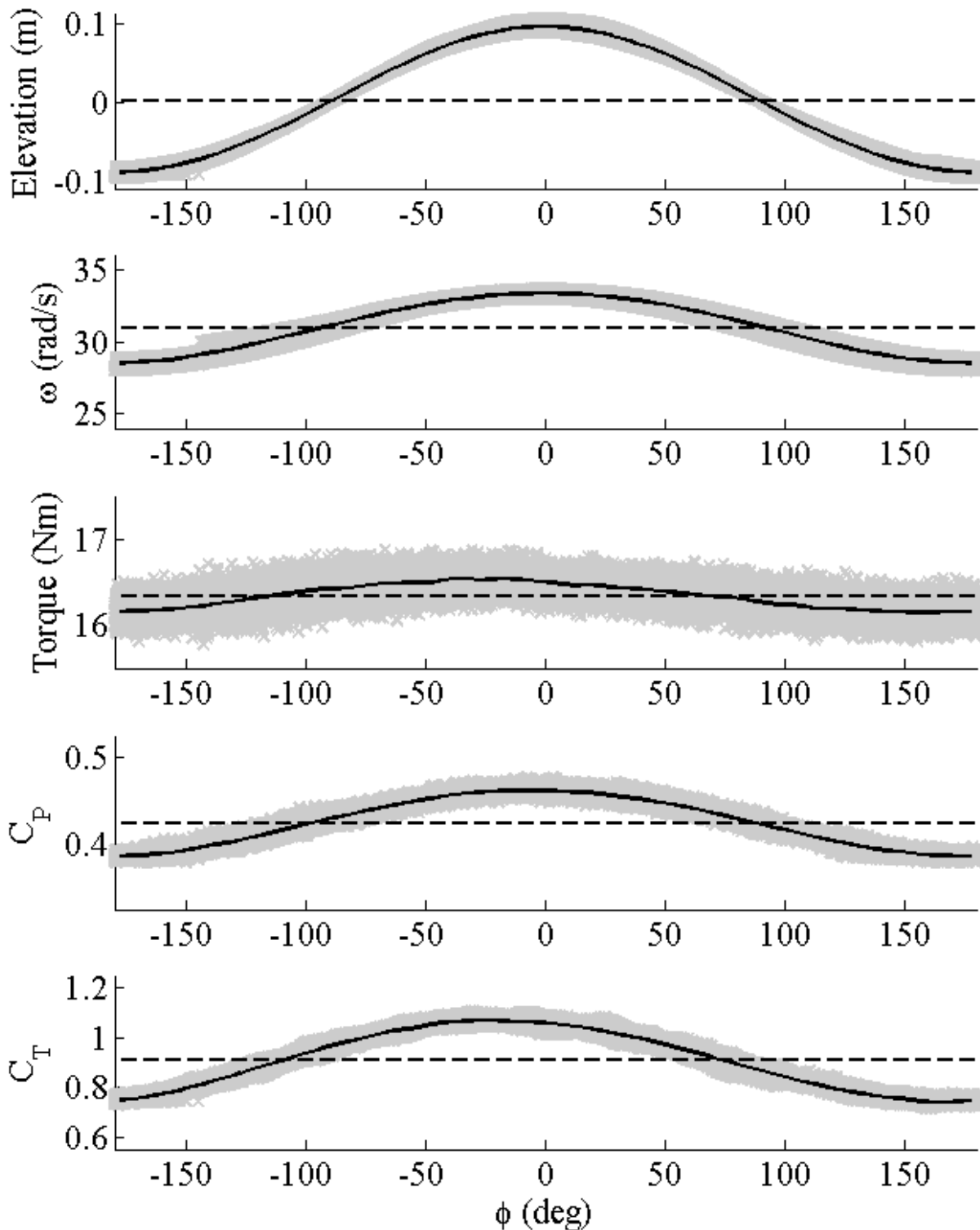
Figure 23: Turbine performance as a function of 0.18 m wave phase at 1.8D tip immersion. Shaft speed, ω, C_P, and C_T varied in phase with wave surface elevation. Torque varied 90° out of phase with the surface elevation of the wave. 0.18 m waves had decreased effects on turbine performance over the wave phase at increased immersion depth. Quantities determined at TSR = 7.37.
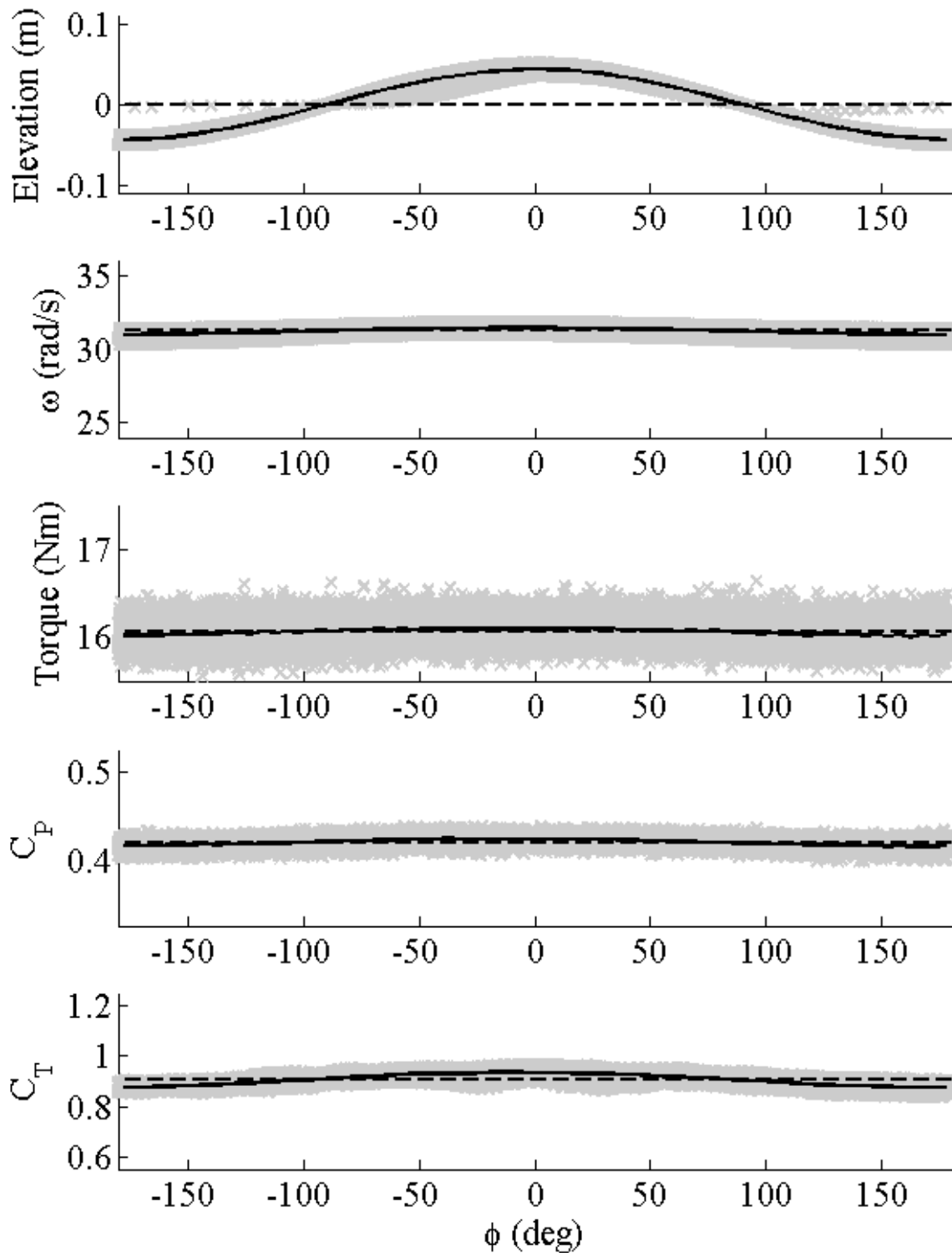
Figure 24: Turbine performance as a function of 0.09 m wave phase at 1.8D tip immersion. Shaft speed, ω, C_P, and C_T varied in phase with wave surface elevation. Torque varied 90° out of phase with the surface elevation of the wave. 0.09 m waves had the smallest effect on turbine performance over the phase of the wave of all conditions tested. Quantities determined at TSR = 7.42.

Tip Immersion Depth	Wave Height m	TSR	TSR Range	ω s^{-1}	ω range s^{-1}	Q N-m	Q range N-m	C_P	C_P range	C_T	C_T range
0.8	0.18	7.25	6.0-8.4 (33%)	30.5	25.2-35.3 (33%)	16.9	16.5-17.5 (6%)	0.43	0.35-0.51 (37%)	0.91	0.55-1.25 (77%)
0.8	0.09	7.45	7.2-7.8 (8%)	31.3	30.2-32.6 (8%)	16.2	15.7-16.7 (6%)	0.42	0.40-0.46 (13%)	0.91	0.77-1.06 (32%)
1.6	0.18	7.37	6.6-8.0 (19%)	31.0	28.0-33.7 (18%)	16.3	15.8-16.9 (7%)	0.42	0.38-0.48 (23%)	0.91	0.71-1.1 (43%)
1.6	0.09	7.42	7.2-7.6 (5%)	31.2	31.0-31.8 (5%)	16.1	15.5-16.6 (7%)	0.42	0.40-0.44 (10%)	0.91	0.84-0.97 (15%)

Table 5: Performance parameters and characteristics for the two immersion depths tested for two types of waves. Percent variation was calculated as the range over the mean value.

G. Near Wake Survey Coordinates Defined

Acoustic Doppler Velocimeters (ADV) were used to measure the three dimensional fluid velocity in the near wake of the turbine. Three axial planes downstream from the turbine rotor for measurements included were X/D = 0.19, 0.57 and 0.95, where D was the turbine diameter. Velocities at two additional planes at X/D = 0.37 and 0.76 were also measured, but not included in the majority of the data presentation that follows. The three planes selected demonstrate the near wake characteristics without the need for two additional planes. For each axial plane, four radial positions were measured at r/D = 0.30, 0.37, 0.43, and 0.49. All measurements were taken in the plane 36° clockwise from vertical plane when viewed from upstream of the turbine. These positions are represented in Figure 27 by the colored 'o' markers in the head on view of the turbine from upstream (left) and the measurement plane 36° from vertical (right).
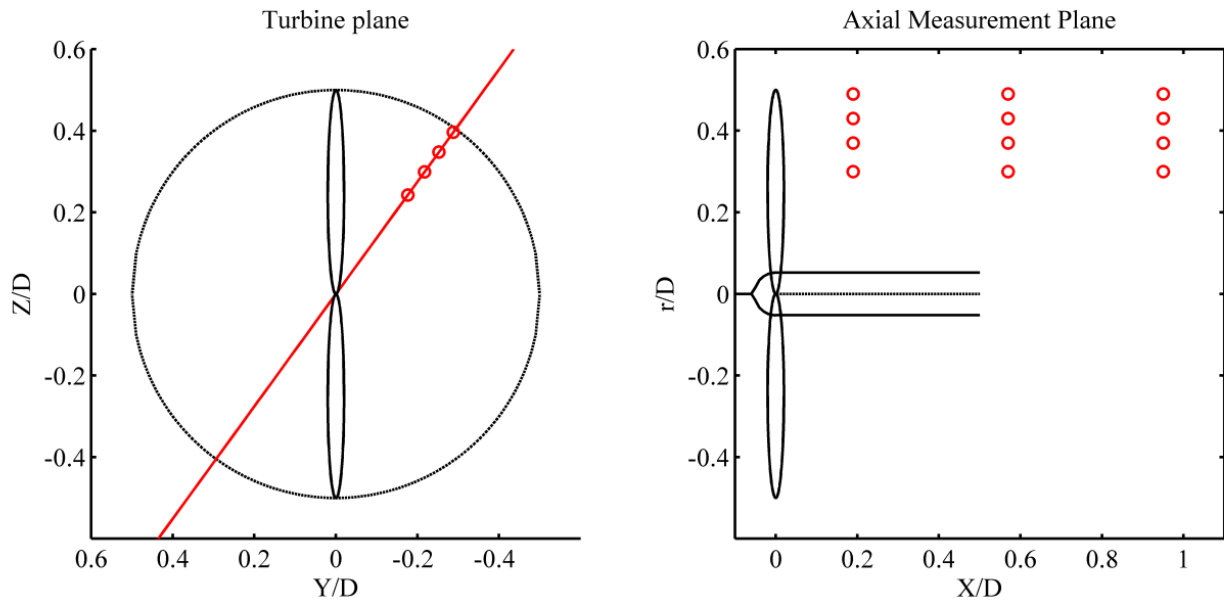

Figure 27: ADV velocity Measurement Locations, *Turbine sizing not to scale.

Nomenclature for the various velocity components is standardized. Two different coordinate systems were utilized: tow tank coordinates and ADV coordinates. The tow tank coordinates were symbolized by X, Y, and Z. Uppercase X was the direction of mean incoming fluid flow as seen by the turbine (the opposite direction of the tow velocity), referenced from the turbine rotor plane as shown in Figure 27b. Uppercase Z was the vertical coordinate, and uppercase Y was the lateral coordinate. The tow tank velocity coordinates were denoted u, v, and w, respectively. This system is pictured in Figure 28. The ADV coordinate system was a cylindrical coordinate system given by r, t, and z. u_r, u_t, and u_z represent the ADV instantaneous velocities in radial, tangential and axial directions, respectively. The ADV coordinates were necessitated by the 36° angle of the reference plane. Consequently, the transformation between tow tank and ADV coordinate systems was a trigonometric relationship, identified in equations 15 through 17.

$$u = -u_z \qquad\qquad 15$$

$$v = -u_r \sin 36 - u_t \cos 36 \qquad\qquad 16$$
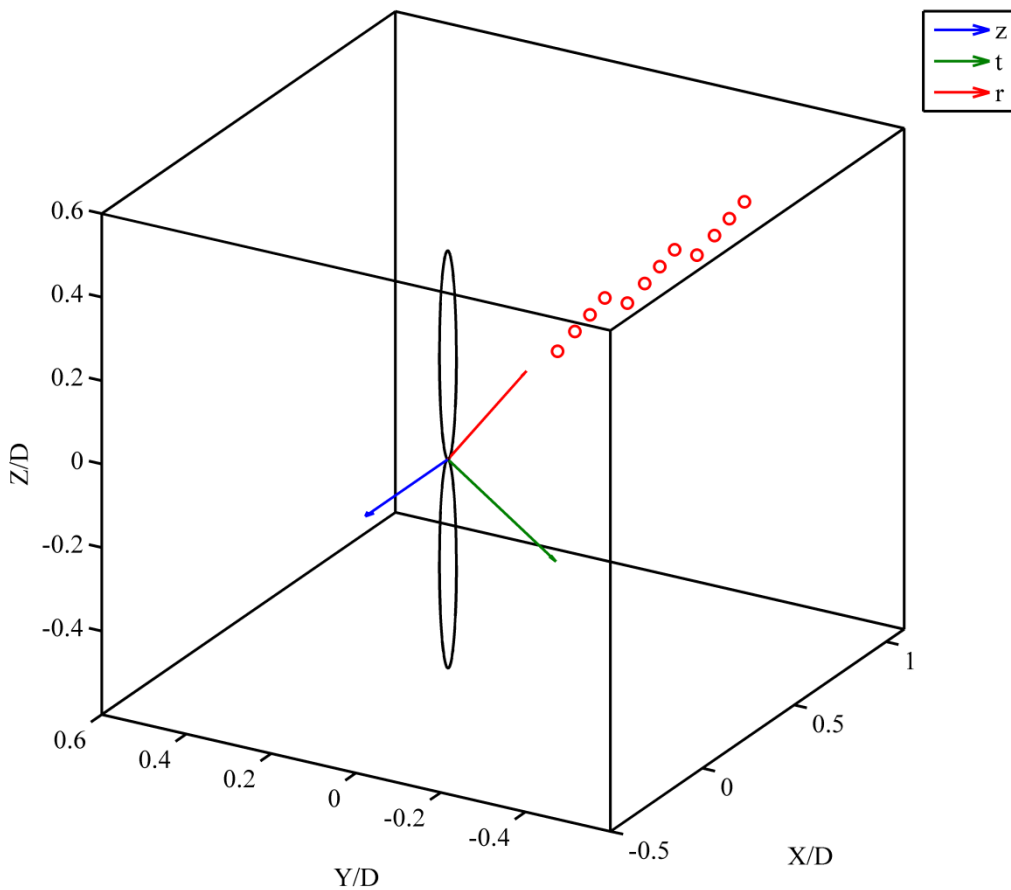
$$w = u_r \cos 36 - u_t \sin 36 \qquad\qquad 17$$

Figure 28: Tow Tank and ADV Coordinate Systems depicted graphically. *Turbine sizing not to scale

H. Near Wake Mean Flow (Steady Inflow Conditions)

Figure 29 shows mean velocity contours in the tow tank coordinate rotor plane (Z-Y) for increasing axial (X) distance downstream of the rotor. Red indicates higher velocities; blue indicates lower velocities. Also included are flow directions indicated by arrows. Mean axial velocity U_z, positive into the paper, U_t, tangential velocity, and U_r, radial velocity, were calculated for the near wake and normalized by the carriage speed U_{tow}. U_z decreased in the streamwise direction (increasing X/D) for all radial locations with magnitudes ranging from 0.55 at r/D = 0.49 to 0.35 at r/D = 0.35.

The largest variation of U_z occurred at the rotor tip, r/D = 0.49 at all axial locations. The variation indicated that the largest component of fluid shear existed at the turbine tip. Fluid shear results in higher localized dissipation of energy.

Radial velocity, U_r, decays with distance from the turbine, while U_t increased as the axial distance increased. U_t had non-uniform distribution with larger magnitudes towards the center of the turbine and smaller magnitudes near the turbine tip. The mean in-plane velocity vector $(U_t^2+U_r^2)^{0.5}$ is also shown and was consistent with a counterclockwise fluid angular momentum resulting from the clockwise rotor rotation, clearly observed at X/D = 0.95. Fluid shear from the in-plane components of velocity was also largest at the turbine tip.
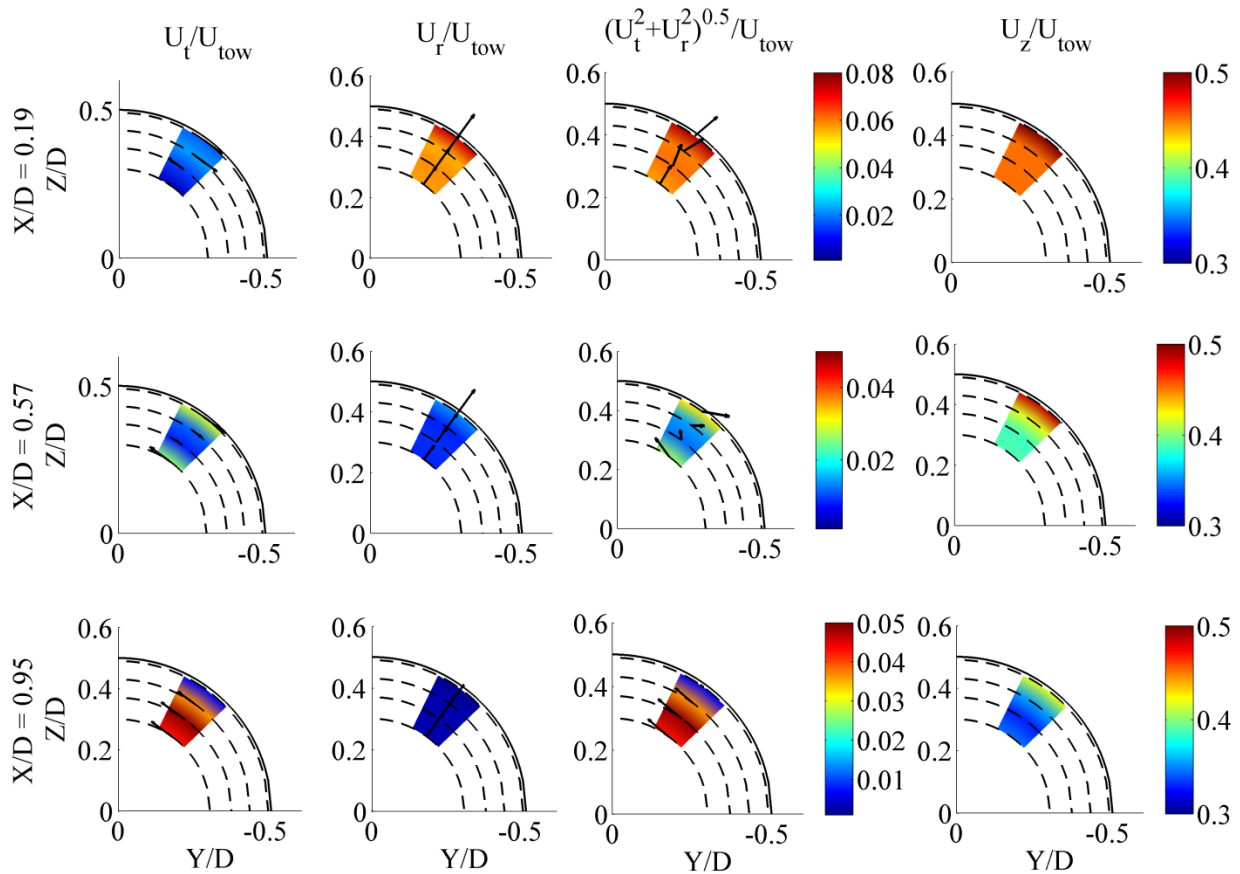

Figure 29: Mean velocities normalized by U_{tow} in three dimensions in the near wake of the turbine. Dashed lines indicate four radial locations, r/D= 0.30, 0.37, 0.43, and 0.49.

I. Near Wake-Turbulence Statistics

Turbulence intensity, I_i, and ratios $\overline{v'^2}\big/\overline{u'^2}$ and $\overline{w'^2}\big/\overline{u'^2}$ are plotted as a function of axial distance

(X/D) in Figure 30 for four radial locations (r/D). Here, primes indicate turbulence fluctuations and overbar indicates time averaging. Turbulence intensity in the axial direction was given by:

$$I_x = \frac{\sqrt{\overline{(u')^2}}}{U_{tow}}$$

18

Turbulence intensity demonstrated rapid decay with the distance from the turbine for all radial locations. At X/D=0.56 reached a value of about 5% of the intensity at X/D = 0.19 at the blade tip radial location r/D=0.49. The other radial locations closer to the turbine center were even lower.

Ratio $\overline{v'^2}\big/\overline{u'^2}$ remains approximately constant within one rotor diameter for all radial locations,

except for a significant increase at X/D=0.95 and r/D=0.3 indicating increased turbulence levels in the lateral direction, consistent with the mean shear of tangential velocity in that area. Ratio $\overline{w'^2}\big/\overline{u'^2}$

appears to have an increasing trend with increasing X/D suggesting that vertical turbulent fluctuations increase in the turbine near wake
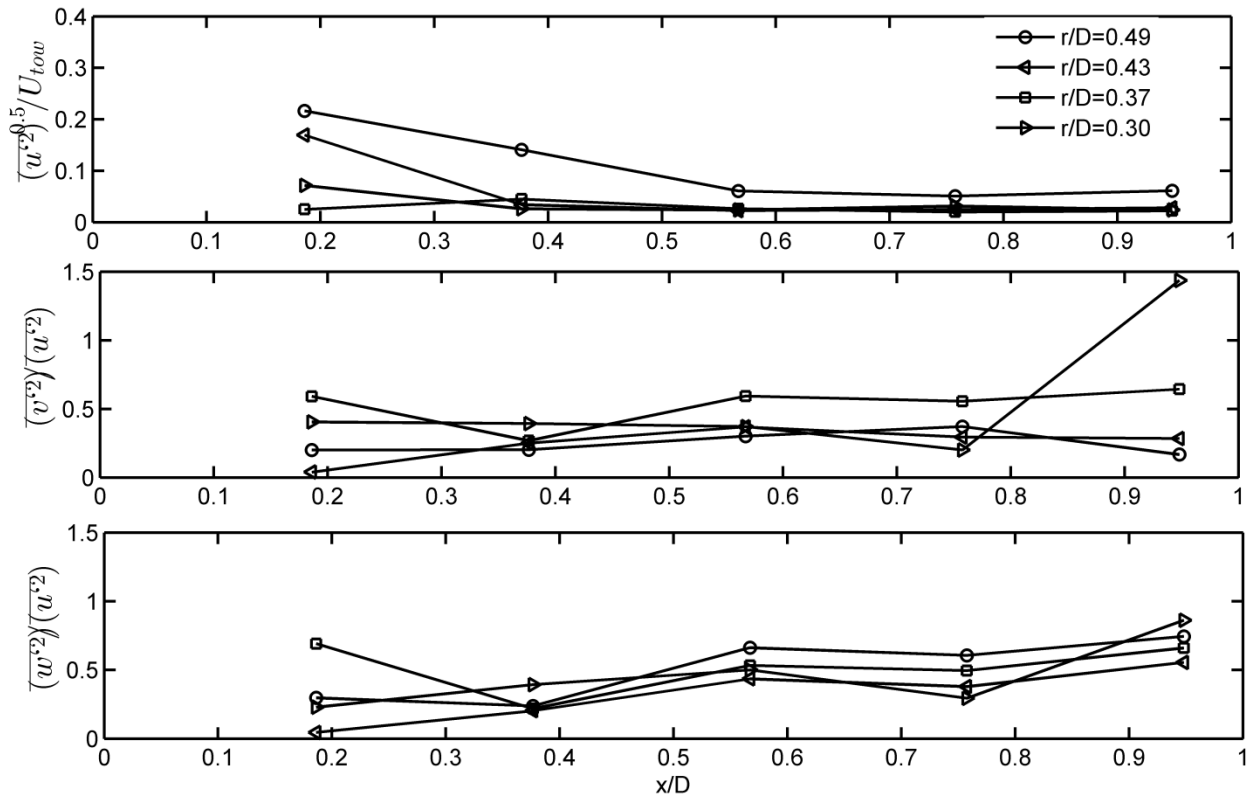

Figure 30: Axial turbulence intensity and ratios of lateral and vertical turbulence variances presented as a function of axial (X/D) distance from the rotor plane. Note that results are plotted for all five axial planes.

In order to further examine turbulence characteristics in the near wake, conditional sampling based on turbine angular position was conducted for the turbulence intensity defined for the x component of velocity as:

$$I_x = \frac{\sqrt{<(u\prime)^2>_\theta}}{U_{tow}}$$

19

Turbulence intensities in the axial, I_x, lateral, I_y, and vertical, I_z, directions were conditionally sampled and plotted as a function of turbine angular position at all radial positions (r/D) for three axial planes (X/D) in Figures 31, 32, and 33.

The mean turbulence intensity was largest in the axial direction and lowest in the lateral direction. The mean turbulence intensity decreased as the axial distance from the turbine plane was increased as shown in Figures 31, 32, and 33. The mean intensity also decreased as the radial position was decreased. In axial plane X/D = 0.19, turbulence intensity decreased from r/D = 0.49 to 0.37, but demonstrated a slight increase from r/D = 0.37 to 0.30. This increase suggests influence from the turbine nacelle. Turbulence intensity at radial location r/D = 0.49 in every axial plane indicated substantial influence from a tip vortex shed at the turbine blades tips. This activity decreased sharply as the sample area of the ADV moved closer to the turbine centerline.

Tip vortex influence was most prevalent at X/D = 0.19, the closest measured plane to the turbine plane pictured in Figure 31. Peaks in the axial turbulence intensity appeared at θ = 110° and 290°. This 180° spacing indicated influence from two turbine blades. The axial component of turbulence intensity was larger than the lateral or vertical components for plane X/D = 0.19. Secondary peaks were observed between the large peaks identified as influence from blade passage in the axial component. The lateral turbulence intensity followed a pattern indicating passage of both turbine blades. The vertical turbulence intensity had a dual peak before and after the peaks in both the radial and tangential components, suggesting the turbine blade passage carried turbulence in front of and behind each blade. The magnitudes of turbulence intensities were significantly smaller at radial locations r/D = 0.43 to 0.30. However, influence from blade passage was still observed in the lateral and vertical components at these positions.

As the axial distance from the turbine was increased, the tip vortex strength decreased. At X/D = 0.57, pictured in Figure 32, the passage of the two blades in each component was still observable at r/D = 0.49. The magnitude of the turbulence spikes was significantly diminished. The secondary peaks observed in the axial component remained. The dual peak pattern in the vertical component was repeated. The pattern observed in the lateral and vertical components at smaller radial locations in plane X/D = 0.19 continued in plane X/D = 0.57. The angular position of the reference blade corresponding to the turbulence peaks was not consistent from plane X/D = 0.19 to X/D = 0.57. The inconsistent timing was a result of the increased axial distance from the reference plane. The turbulence intensity in the wake moves with the axial fluid velocity. Therefore, the shift in the timing of the turbulence intensity peaks corresponds to the axial fluid velocity and the distance from X/D = 0.19 to X/D = 0.57.

In plane X/D = 0.95, the signature of tip vortex continued to deteriorate. The secondary peaks observed in the axial component at r/D = 0.49 disappeared. Dual peaks were not observed in the vertical component. The lateral and vertical components did not exhibit the periodic turbulence intensity peaks identified as blade passage at positions r/D = 0.37 and 0.30. Position r/D = 0.43 demonstrated this pattern in the axial and vertical components, but not the lateral component. The changes observed between Figures 31, 32, and 33 indicated an introduction of turbulence to the flow from the turbine blades. This turbulence quickly dissipated in the near wake of the turbine.
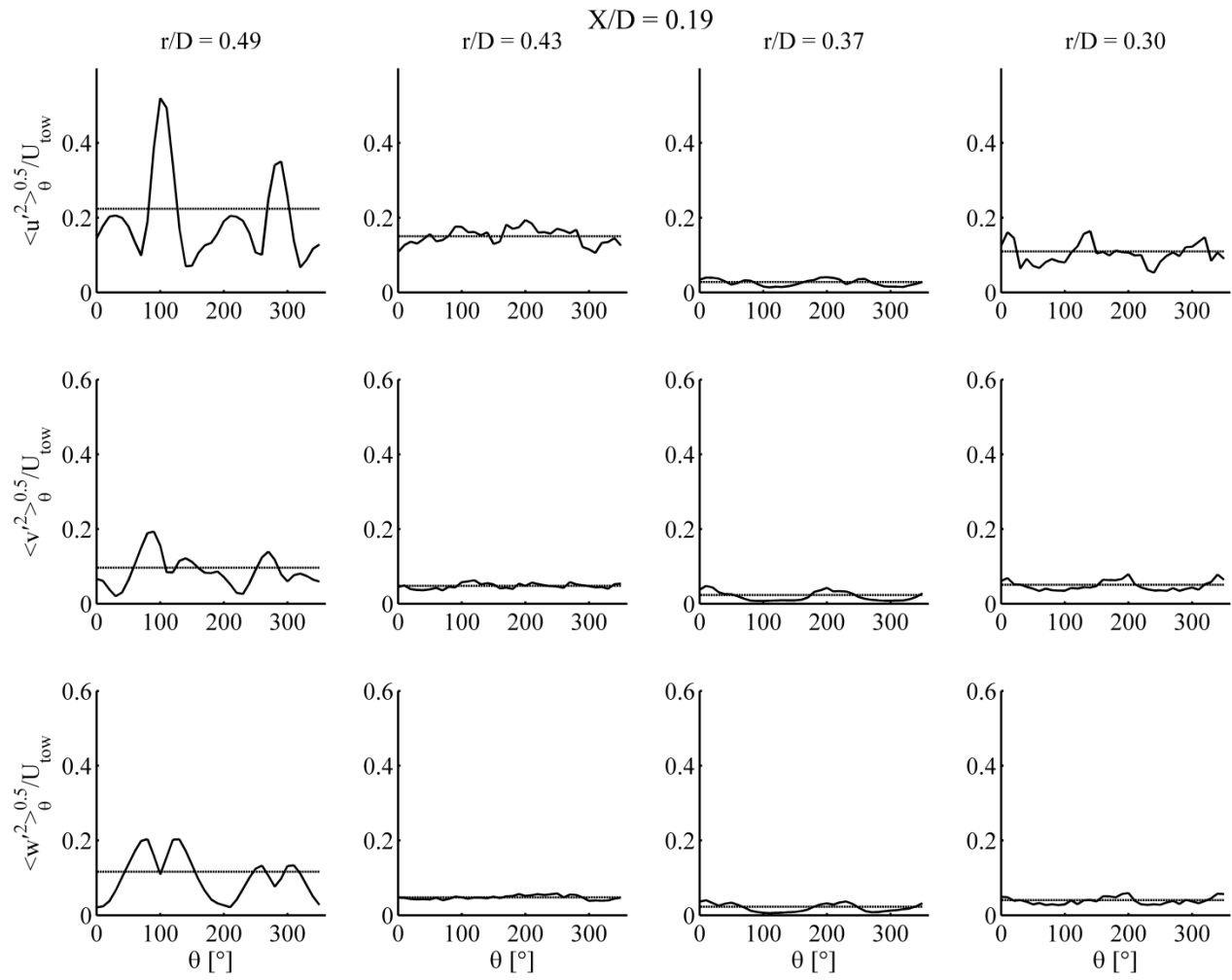
Figure 31: Conditionally Sampled Turbulence Intensity at X/D = 0.19. Mean values for each position are indicated by the solid horizontal line.
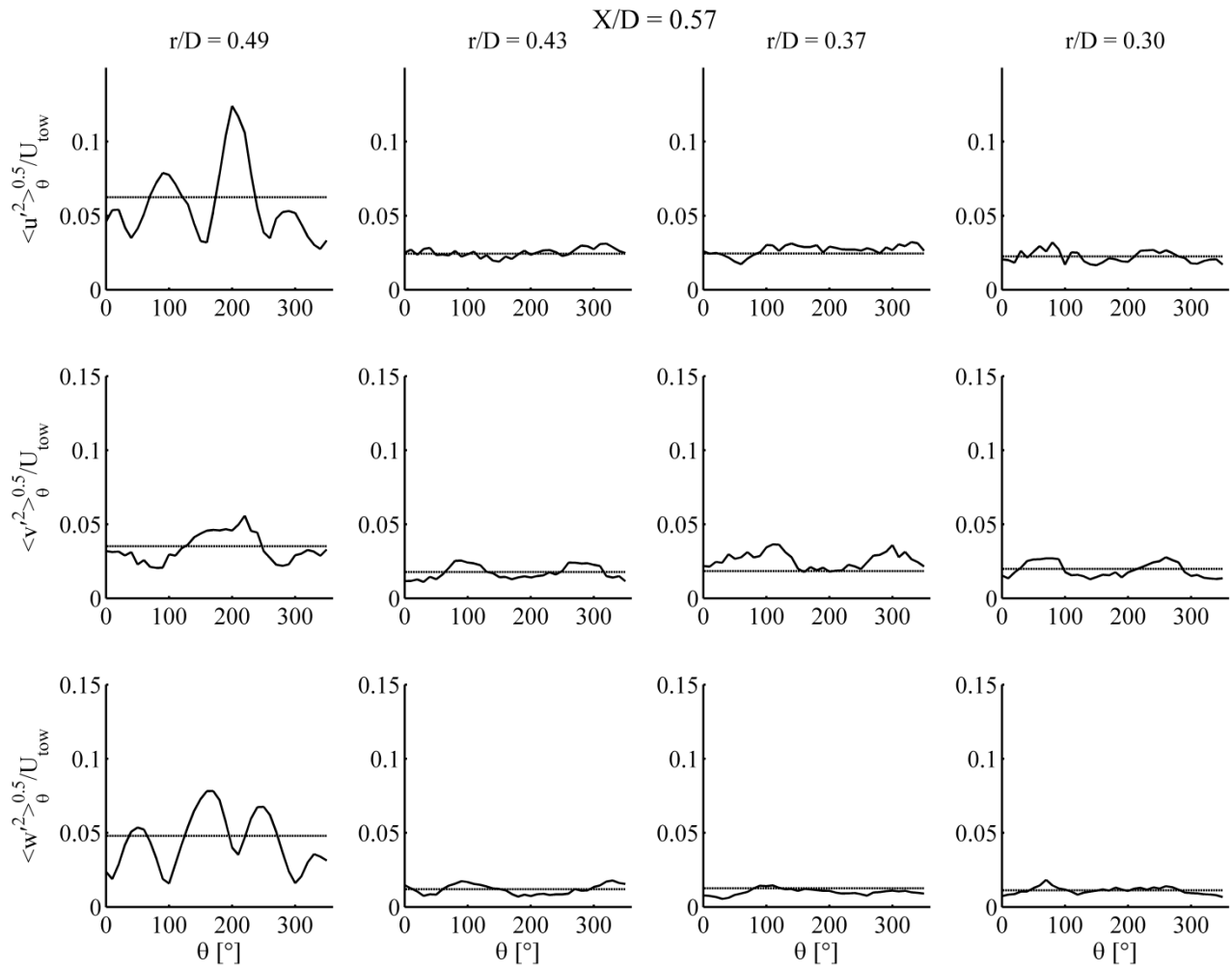
Figure 32: Conditionally Sampled Turbulence Intensity at X/D = 0.57. Mean values for each position are indicated by the solid horizontal line.
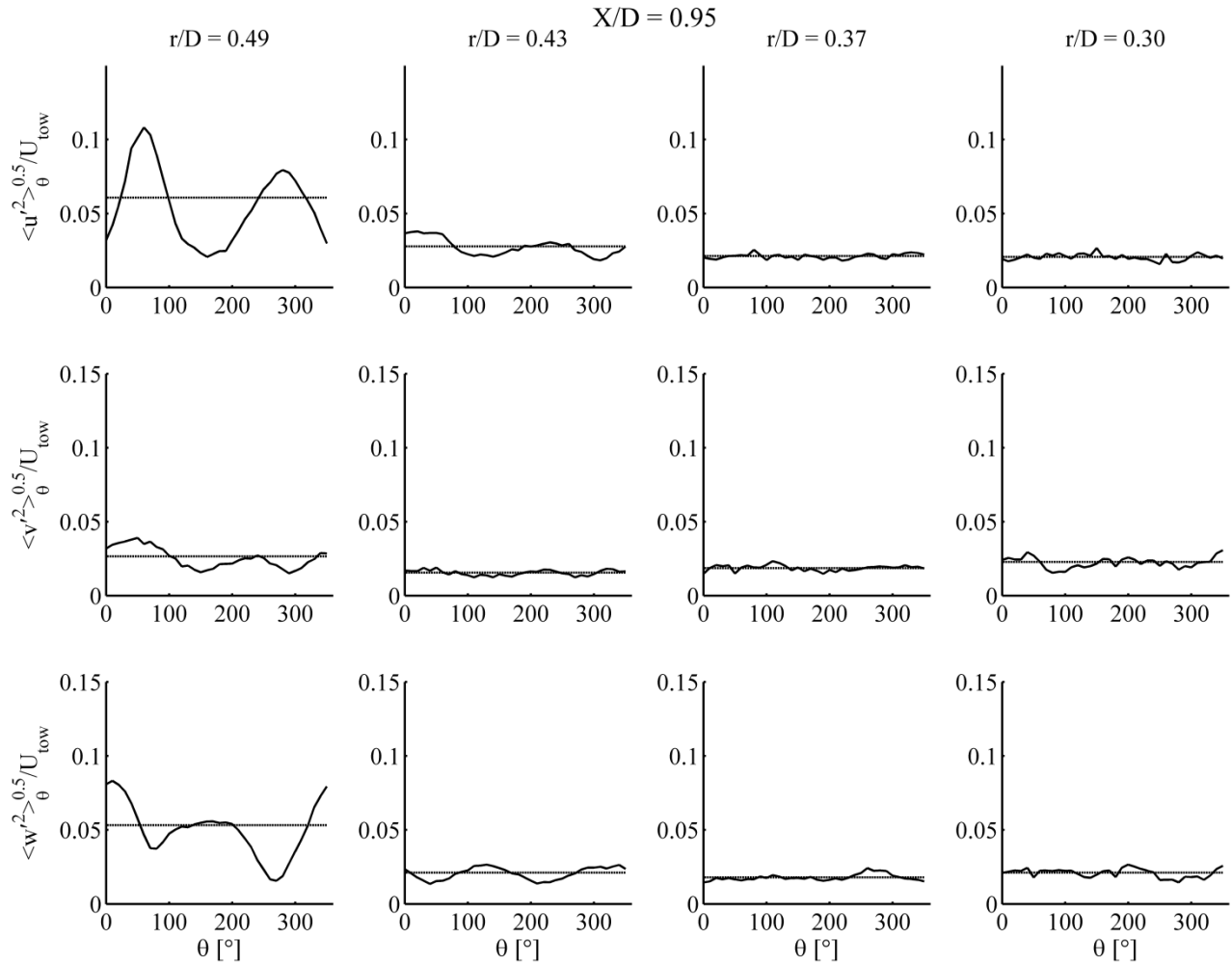
Figure 33: Conditionally Sampled Turbulence Intensity at X/D = 0.95. Mean values for each position are indicated by the solid horizontal line.

The same process described for conditionally sampled turbulence intensities is repeated for the normalized Reynolds shear stress defined as:

$$\frac{-<u'w'>_\theta}{U_{tow}^2}$$

20

The Reynolds shear stress was an indicator of turbulent shear in the near wake. The shear was largest at the rotor tip at the closest axial plane (X/D = 0.19) as well as in other planes downstream from the rotor. This was consistent with the mean flow velocities which demonstrated the highest shear at r/D = 0.49. The highest shear for all axial locations was located at r/D = 0.49. The shear quickly dissipated as the axial distance was increased. The Reynolds shear stress at r/D = 0.49 demonstrated a periodicity consistent with blade passage. At X/D = 0.19, the leading and trailing edge of the blade passage is noticeable. At X/D = 0.57, the leading and trailing edges of the blades are observable, but less distinct. By X/D = 0.95, only the blade passage is observable. The influence from the leading and trailing edges of the blades is no longer apparent.

The Reynolds shear stresses were elevated in plane X/D = 0.19. At radial positions below r/D = 0.49, blade position had no effect on the Reynolds shear stress. For radial positions below r/D = 0.49

in planes X/D = 0.57 and 0.95, the stress was negligible. Slight periodicity was observed for r/D = 0.43 at X/D = 0.95, indicating the expansion of the tip vortex observed at r/D = 0.49.
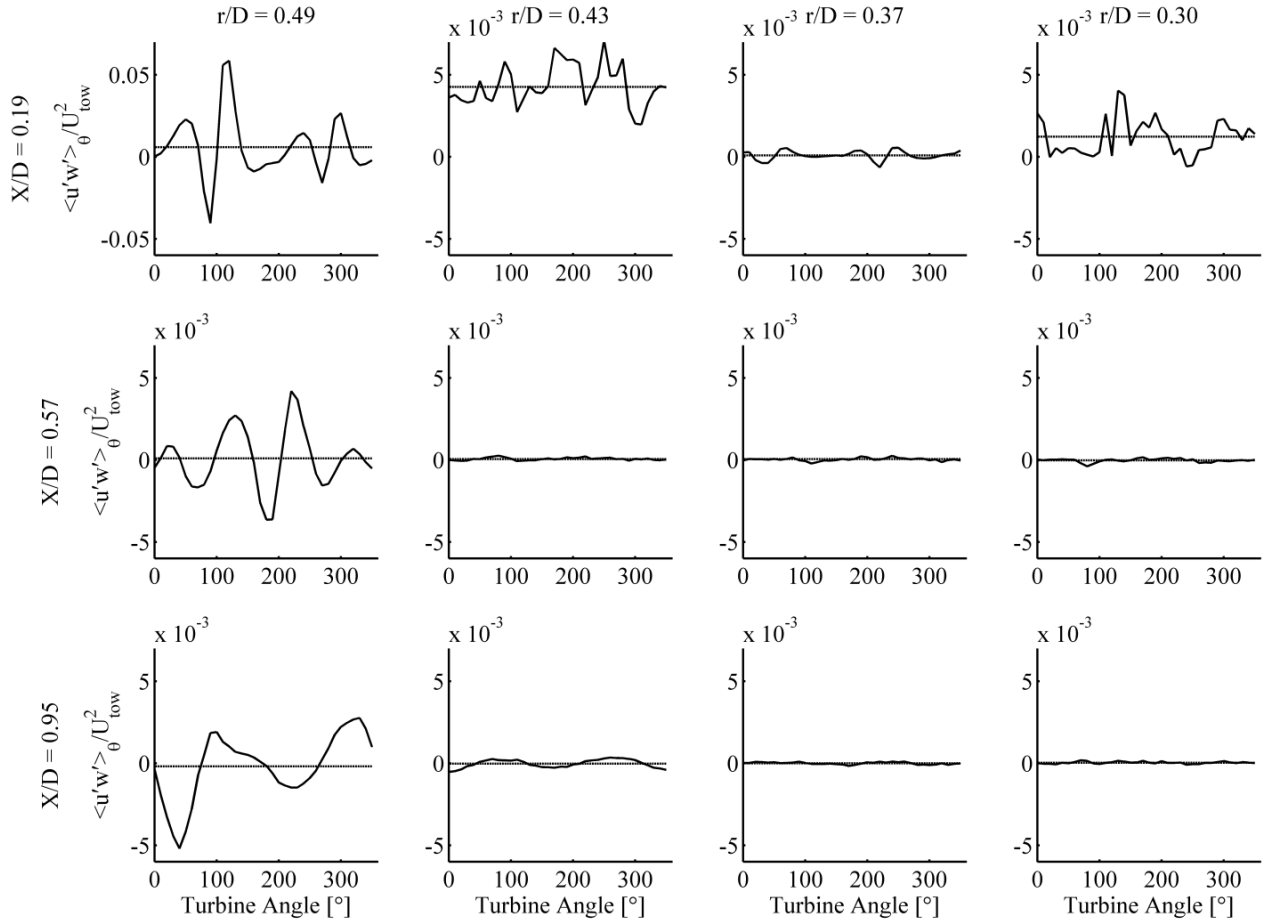

Figure 34: Conditionally sampled Reynolds shear stresses, $\frac{-<u'w'>_\theta}{U_{tow}^2}$, for each position measured in the wake. Note the scale is a factor of 10 larger for X/D = 0.19, r/D = 0.49, where the Reynolds shear stress was significantly larger. The solid horizontal line represents the average stress, $\frac{-\overline{u'w'}}{U_{tow}^2}$.

Conditional sampling described above utilized the Z-pulse and the methodology described in Section 2F. The TSR was constant at 7.2 for all wake survey runs. Only the location of the ADV sensor was varied. For all the runs conducted at X/D = 0.19, the standard deviation of the rotational speed ranged from 0.15 to 0.38 rad/s. The variance of the rotational speed did not exceed 0.5% of the mean rotational speed for steady state conditions. This confirms the assumption that the rotational speed was constant for each run.

The number of samples used for averaging the conditionally sampled results varied from run to run. The number of samples used for each ADV position is listed in Table 5 with variations related to the quality of the ADV signal. The quality of the ADV signal depended on the number of seeding particles in the tow tank. In the ADV data analysis, only data with high correlation (>70%) were used in the analysis. To verify conditional sampling convergence even with the lowest number of samples, the running average of the turbulence intensity was plotted as a function of the number of

samples, n, included in the average. The lowest number of samples, 56, was observed at positions X/D= 0.57 and 0.95 for r/D= 0.30. A convergence study for these two runs is depicted in Figures 35 and 36 respectively. θ = 90° was selected as the turbine angular position for this demonstration. The convergence study was repeated for the run with the largest number of samples in Figure 37. In addition to the variance from run to run, the number of samples used for the average value of each angle varied within each run. This difference from angle to angle was a result of patches of poor correlation in the ADV signal that were discarded within the run. This caused some angles to have one or two additional or fewer samples in the average. Overall, convergence study suggests that conditionally sampled turbulence intensities converge and reach stable values within the number of samples available.

X/D	r/D			
	0.49	0.43	0.37	0.30
0.19	157	86	151	75
0.57	114	77	100	**56**
0.95	143	146	110	**56**

Table 5: Number of samples included in the average for conditional sampling based on turbine angular position. The lowest number of samples, 56, was observed at positions X/D= 0.57 and 0.95 for r/D= 0.30.
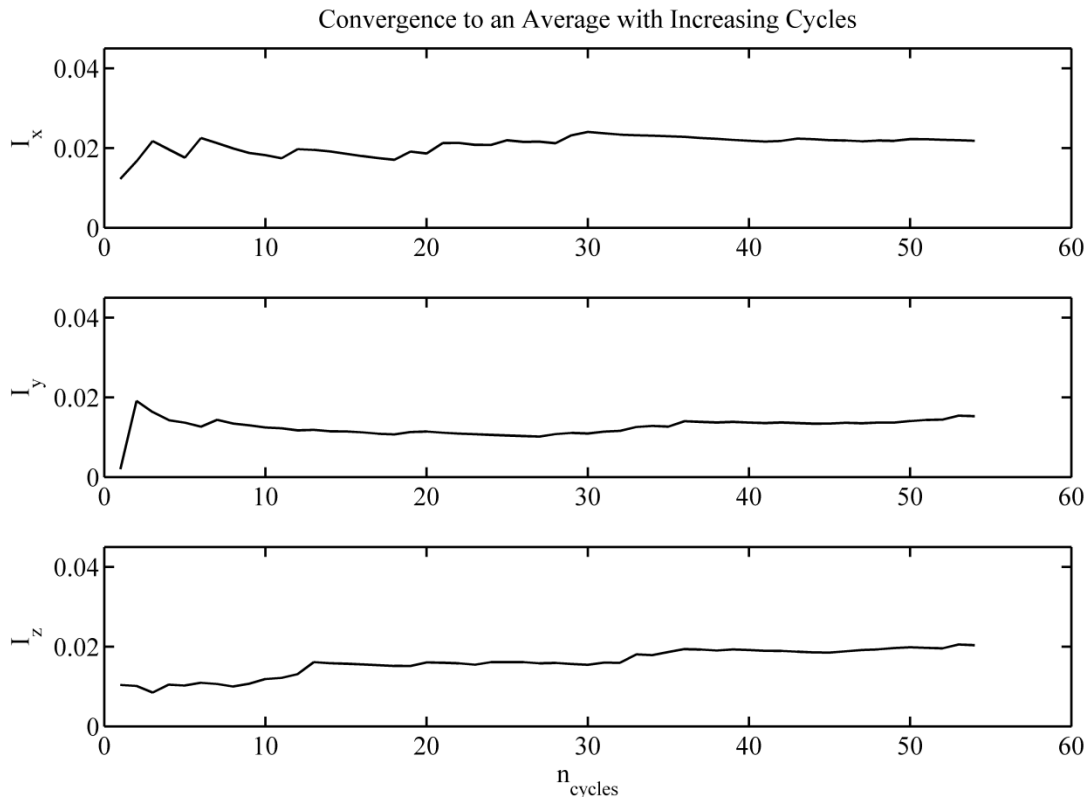

Figure 35: Running average of the turbulence intensities at X/D = 0.57, r/D = 0.30 over 56 samples. Convergence shown is for θ = 90° for this study. Convergence is achieved for each quantity within 30 conditionally sampled data points.
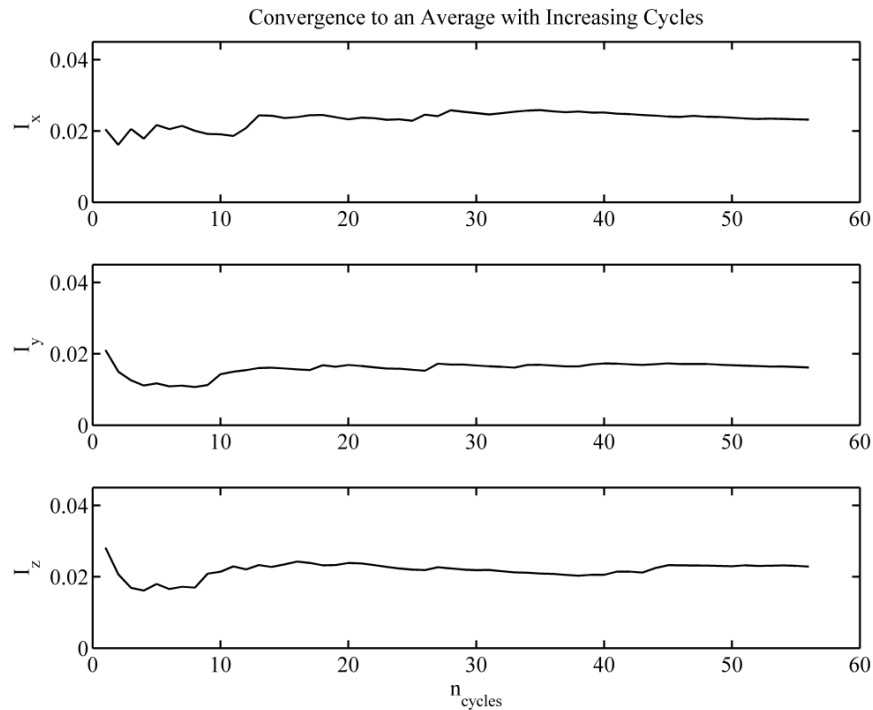
Figure 36: Running average of the turbulence intensity in three dimensions at X/D = 0.95, r/D = 0.30 over 56 samples. Convergence shown is for θ = 90° for this study. Convergence is achieved for each quantity within 20 conditionally sampled data points.
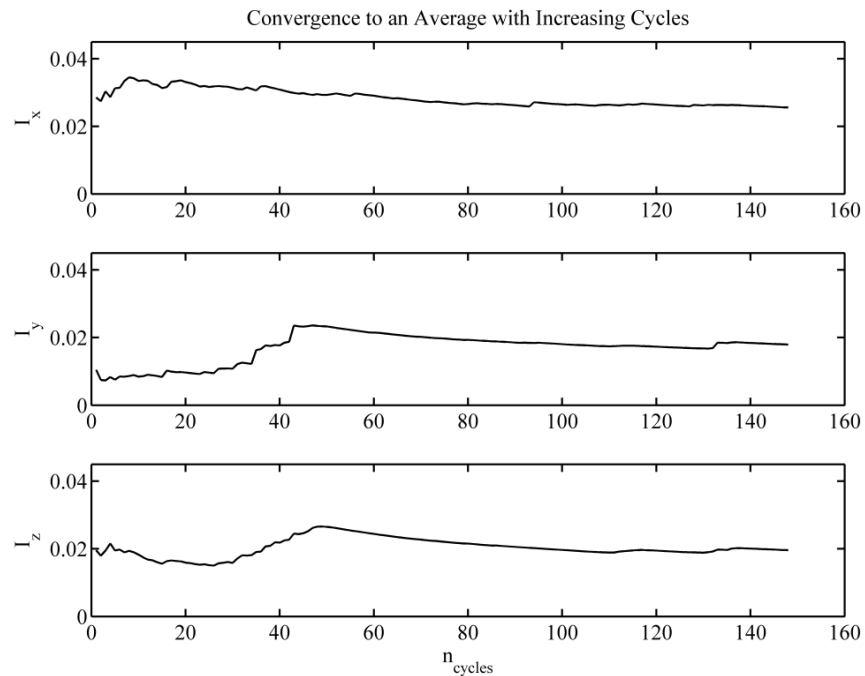

Figure 37: Running average of the turbulence intensity in three dimensions at X/D = 0.19, r/D = 0.37 with 151 samples. Convergence shown is for θ = 90° for this study. At this angle, only 148 samples existed with sufficient correlation.

IV.   Conclusions

A 1/25th scale model tidal turbine was tested under steady and unsteady flow conditions at two different immersion depths. The two waves included intermediate water waves (H/λ = 0.6) and deep water waves (H/λ = 1.2) scaled to represent waves experienced by tidal turbines deployed in the field. The data were presented as time averages, phase averages with respect to waves, and conditional averages based on turbine position. The near wake velocities of the model turbine were measured using Acoustic Doppler Velocimetry. Mean velocities and turbulence characteristics in the near wake were quantified. The following conclusions were drawn:

1. Rotor tip immersion depths of 0.8D and 1.8D did not affect performance characteristics for steady flow conditions. C_P and C_T were not affected by immersion depth over the TSR range tested during experimentation. C_T experienced increased variations at TSR > 8.6 as a result of cavitation. At 0.8D tip immersion depth, cavitation lowered $<C_T>_\theta$ when θ= 270°. At the same depth, $<C_T>_\theta$ experienced an increase when θ= 90°. When the tip immersion depth was increased to 1.8D, $<C_T>_\theta$ was lower than the mean at θ = 180° due to cavitation. $<C_T>_\theta$ was larger than the mean when θ = 0°.

2. The presence of surface gravity waves did not have a significant effect over average performance characteristics. However, the tests conducted at 0.8D tip immersion with 0.18m waves exhibited slightly higher average power and thrust coefficient than those without waves. The possible cause for this is increased net forward velocity of the water due to Stokes drift. The influence from Stokes drift was modeled and compared to experimental results. The Stokes drift explanation appeared to match experimental results.

3. Phase averaged performance characteristics demonstrated significant variation with type of wave and rotor immersion depth. The borderline intermediate to deep water wave, as defined by relative depth (h/λ = 0.6), had a larger effect on phase averaged performance characteristics than the purely deep water wave. The borderline intermediate to deep water wave had larger water velocity magnitudes than the deep water wave as predicted by the second order Stokes wave model [11]. The increased velocity magnitudes caused larger effects on phase averaged performance characteristics. Increased immersion depth resulted in decreased influence on turbine performance characteristics from both waves tested. Deeper immersion depths placed the turbine lower in the water column, resulting in less influence from surface waves.

4. Waves led to cyclic loading and unsteady power generation. The rotational speed of the turbine, ω, the power coefficient, C_P, and the thrust coefficient, C_T, varied in phase with the wave surface elevation. The torque was 90° out of phase with the wave surface elevation. Over the wave phase, C_T varied as much as 77% of the average C_T for the run. Cyclic loading is a major design concern. Fatigue failure modes become a limiting factor in tidal turbine design. C_P varied as much as 37% of the average C_P. The unsteady power generation leads to poor power quality produced by an electric generator, reducing the effectiveness of tidal turbines.

5. Mean wake velocities were consistent with counterclockwise fluid angular momentum for a clockwise rotor rotation. The counterclockwise angular momentum in the wake data was clearly observed at one diameter downstream from the rotor plane. The counterclockwise angular momentum is consistent with a clockwise turbine rotation, when viewed from upstream, due to conservation of momentum.

6. The largest axial velocity mean shear occurs at the blade tip for all downstream measurement locations. The mean shear was represented by the change in mean axial velocity, U_z, over the change in radial location (r/D).

7. Wake turbulence intensity decayed significantly within one rotor diameter. By axial plane X/D = 0.57, the wake turbulence intensity was within 5% of turbulence measured at X/D = 0.19.

8. Conditional sampling of turbulence intensity and Reynolds shear stress suggested presence of tip vortex close to the blade tips and its decay downstream from the rotor plane.

V. Future Work

Future work with these data sets obtained as a part of this Trident project will concentrate on the near wake data analysis with waves, specifically looking at the influence of waves on the mean wake velocities and the wake turbulence. This is important when considering placing multiple turbines in an array. Furthermore, these data sets provide valuable insight into near wake structure and indicate that better spatial coverage of measurements in the wake are needed, especially close to the blade tips. The use of Particle Image Velocimetry (PIV) is currently being considered as a technique to obtain more detailed data in the turbine near wake.

VI.   References

[1]   Cummins, P. and Garrett, C. Generating Power from Tidal Currents. *Journal of Waterway, Port, Coastal, and Ocean Engineering*, **130**, No. 3. May 2004. pp 114-118.

[2]   Falnes, J. Wave-Energy Conversion Through Relative Motion Between Two Single-Mode Oscillating Bodies. Journal of Offshore Mechanics and Artic Engineering, **121**, Iss. 1. February 1999. pp 32 - 39.

[3]   Tides and Currents. National Ocean and Atmospheric Administration. 21 December 2011. http://tidesandcurrents.noaa.gov/.

[4]   Mabus, R. Address given at Naval Energy Forum. McLean, Virginia. 14 October 2009.

[5]   Huebsch, W., Munson, B., Okiishi, T., Young, D. Fundamentals of Fluid Mechanics Sixth Edition. John Wiley & Sons. 2009.

[6]   Taylor, P., Seagen Tidal Power Installation. Alternative Energy. 6 June 2007. http://www.alternative-energy-news.info/seagen-tidal-power-installation/.

[7]   SeaGen. Marine Current Turbines Turning the Tide. http://www.marineturbines.com/.

[8]   Baltrop, N., Varyani, K.S., Grant, A, Clelland, D., Pham, X.P., 2007. Investigation into wave-current interactions in marine current turbines. Proceedings of the IMECHE Part A: *Journal of Power and Energy*, **221**, 223-242.

[9]   Luznik, L., Flack, K.A., Lust E.E, Taylor, K., 2013. The Effect of Surface Waves on the Performance Characteristics of a Model Tidal Turbine, *Renewable Energy*, **58**, pp 108-114.

[10]   Luznik, L and Flack, K, 2010. Observations of turbulent flow fields in the Chesapeake Bay Estuary for tidal energy conversion. In OCEANS 2010, 1-5.

[11]   Dean, G.R., Dalrymple A.R. 1991. Water Wave Mechanics for Engineers and Scientists. World Scientific Publishing Co.

[12]   Request for Proposal, Department of Energy, Marine hydrokinetic energy reference turbine laboratory studies, 2011.

[13]   Miley, S.J., A catalog of low Reynolds number airfoil data for wind turbine applications, 3387, 1982.

[14]   Bossanyi, Ervin, Burton, Tony, Jenkins, Nick, and Sharpe, David. 2001. Wind Energy Handbook. John Wiley & Sons, LTD., pp. 45.

[15]   Bahaj, A.S., Molland, J.R., Chaplin, J.R., Batten, W.M.J, 2007. Power and thrust measurements of marine current turbines under various hydrodynamic flow conditions in a cavitation tunnel and a towing tank. *Renewable Energy* **32**, pp. 407-426.

[16]   Absolute Encoders. Sick Stegmann. Dayton, Ohio. pp. 12.

[17]   Vectrino: 3D Water Velocity Sensor Lab Probe. Rud, Norway. pp 4.

[18]   Lust, E, Walker, J, Luznik, L, Flack, K, and Van Benthem, M. The Influence of Surface Gravity Waves on Marine Current Turbine Performance. Submitted to the European Wave and Tidal Energy Conference.

[19]   J. S. Bendat and A.G. Piersol, Random Data: analysis and measurement procedures, Wiley &Sons, Inc., 566 pp, 1986.

[20]   N.E. Huang, Z. Shen, S. R. Long, M. C. Wu, H. H. Shih, Q. Zheng, N. Yen, C. C. Tung, H. H. Liu. The empirical mode decomposition and the Hilbert spectrum for nonlinear and non-stationary time series analysis, Proc. R. Soc. Lond. A 454, (1998) pp. 903-995.

[21]   N.E. Huang, A new view of non-linear water waves: the Hilbert spectrum, Annu. Rev. Fluid Mech. 31 (1999) pp. 417–457.